

Contactless Arterial Blood Pressure Waveform Monitoring with mmWave Radar

QINGYONG HU, The Hong Kong University of Science and Technology, Hong Kong SAR

QIAN ZHANG*, The Hong Kong University of Science and Technology, Hong Kong SAR

HAO LU, The Hong Kong University of Science and Technology (Guangzhou), China

SHUN WU, The Chinese University of Hong Kong, Hong Kong SAR

YUXUAN ZHOU, The Hong Kong University of Science and Technology, Hong Kong SAR

QIANYI HUANG, Sun Yat-sen University, China

HUANGXUN CHEN, The Hong Kong University of Science and Technology (Guangzhou), China

YING-CONG CHEN, The Hong Kong University of Science and Technology (Guangzhou), China

NI ZHAO, The Chinese University of Hong Kong, Hong Kong SAR

Arterial blood pressure waveform (ABPW) offers comprehensive insights into cardiovascular health compared to discrete blood pressure measurements. However, accurately estimating shapes and pressure values of ABPW points in a beat-to-beat manner poses significant challenges. Current ABPW monitoring methods require invasive procedures or continuous skin contact, which are inconvenient and unsatisfactory. Thus, we propose WaveBP, the first contactless ABPW monitoring system utilizing a commercial mmWave radar, driven by the understanding that cardiac information serves as an implicit bridge between mmWave signals and AWPB based on a hemodynamics analysis model. To preserve waveform details, we design a hybrid Transformer model called mmFormer, incorporated with spatially-informed shortcuts. mmFormer enables consistent sequence-to-sequence transformations while accommodating different levels of personalization efforts. To mitigate the inherent instability of mmWave signals, we develop a beamforming-based data augmentation approach that has been empirically and theoretically proven to enhance robustness with multiple spatial observations. Additionally, we introduce a cross-modality knowledge transfer framework to fuse knowledge from cardiac modalities (ECG/PPG) with vibrations captured in mmWave reflections, improving accuracy without requiring extra deployment overhead. Extensive evaluations conducted on 43 subjects using a leave-one-subject-out setup validate that WaveBP achieves a high waveform correlation of 0.903 and exhibits a low (mean \pm standard deviation) error of point-level measurements at (-0.14 \pm 7.48) mmHg, which could be further reduced by subject-specific specialization. WaveBP demonstrates remarkable performance under challenging scenarios and exhibits potential for detailed cardiac estimations, as evidenced by our case studies on relative cardiac output estimation and cardiac abnormality detection.

*Qian Zhang is the corresponding author.

Authors' Contact Information: **Qingyong Hu**, qhuag@cse.ust.hk, The Hong Kong University of Science and Technology, Hong Kong SAR; **Qian Zhang**, qianzh@cse.ust.hk, The Hong Kong University of Science and Technology, Hong Kong SAR; **Hao Lu**, hlu585@connect.hkust-gz.edu.cn, The Hong Kong University of Science and Technology (Guangzhou), China; **Shun Wu**, 1155152220@link.cuhk.edu.hk, The Chinese University of Hong Kong, Hong Kong SAR; **Yuxuan Zhou**, yzhoudu@connect.ust.hk, The Hong Kong University of Science and Technology, Hong Kong SAR; **Qianyi Huang**, huangqy89@mail.sysu.edu.cn, Sun Yat-sen University, China; **Huangxun Chen**, huangxunchen@hkust-gz.edu.cn, The Hong Kong University of Science and Technology (Guangzhou), China; **Ying-Cong Chen**, yingcongchen@ust.hk, The Hong Kong University of Science and Technology (Guangzhou), China; **Ni Zhao**, nzhao@ee.cuhk.edu.hk, The Chinese University of Hong Kong, Hong Kong SAR.

Permission to make digital or hard copies of all or part of this work for personal or classroom use is granted without fee provided that copies are not made or distributed for profit or commercial advantage and that copies bear this notice and the full citation on the first page. Copyrights for components of this work owned by others than the author(s) must be honored. Abstracting with credit is permitted. To copy otherwise, or republish, to post on servers or to redistribute to lists, requires prior specific permission and/or a fee. Request permissions from permissions@acm.org.

© 2024 Copyright held by the owner/author(s). Publication rights licensed to ACM.

ACM 2474-9567/2024/12-ART178

<https://doi.org/10.1145/3699781>

CCS Concepts: • Human-centered computing → Ubiquitous and mobile computing systems and tools; • Applied computing → Health informatics.

Additional Key Words and Phrases: Arterial blood pressure waveform, contactless sensing, mmWave, neural network

ACM Reference Format:

Qingyong Hu, Qian Zhang, Hao Lu, Shun Wu, Yuxuan Zhou, Qianyi Huang, Huangxun Chen, Ying-Cong Chen, and Ni Zhao. 2024. Contactless Arterial Blood Pressure Waveform Monitoring with mmWave Radar. *Proc. ACM Interact. Mob. Wearable Ubiquitous Technol.* 8, 4, Article 178 (December 2024), 29 pages. <https://doi.org/10.1145/3699781>

1 INTRODUCTION

Blood pressure (BP) monitoring is vital to assess the health status of the heart and cerebral vessels. While discrete systolic/diastolic blood pressure (SBP/DBP) values are commonly measured, they are insufficient for detailed assessment of cardiac indicators (e.g., stroke volume, cardiac output (CO), and vascular resistance) [9], which are associated with prevalent cardiac diseases like heart failure and cardiogenic shock [33, 61] that affect more than 64 million people around the world [49]. Beyond discrete values, the arterial blood pressure waveform (ABPW) contains finer-grained information that depicts the complete cardiac cycle, including the rise of blood pressure due to the blood ejection in the systole stage, the descent at the closure of the aortic valve, and the trough state when blood flows out of the aorta [9] as shown in Figure 1. With detailed BP variations inside heartbeats, ABPW can also depict abnormalities with internal cardiovascular statuses beyond discrete BP values, some of which may not even be reflected in ECG signals [38]. Figure 2 shows several cases of cardiac abnormalities that may have similar discrete BP values but behave quite distinctly in ABPW. Continuous ABPW monitoring is significant for assessing the overall cardiovascular status to help diagnose relevant cardiac diseases [2].

However, existing methods do not fully meet the requirement of accurate and convenient AWPW monitoring. The arterial catheter-based method [45] inserts a tube into blood vessels. It is a clinical gold standard method but is limited to intensive care unit (ICU) scenarios due to its invasiveness. For non-invasive methods, some prior works, including cuff-based auscultatory and oscillometric methods [5], wearable methods [6, 7], contactless solutions [24, 35, 52, 60], etc., estimate discrete SBP/DBP values as coarse approximations of AWPW, missing essential information on variation trends. Nonetheless, existing contactless solutions [8, 28, 35, 52, 54, 60] all fail to achieve continuous AWPW monitoring as shown in Table 1, because they require a period of clean signals (several cardiac cycles) to summarize one discrete result based on the pulse transit time (PTT) methodology [42]. AWPW monitoring is more challenging than discrete measurements, as an accurate AWPW approach requires preserving both the AWPW point pressure values and the overall waveform shape. Recently, some progress, including the volume clamp method [41] and wearable methods [17, 26] has been made to obtain AWPW in a

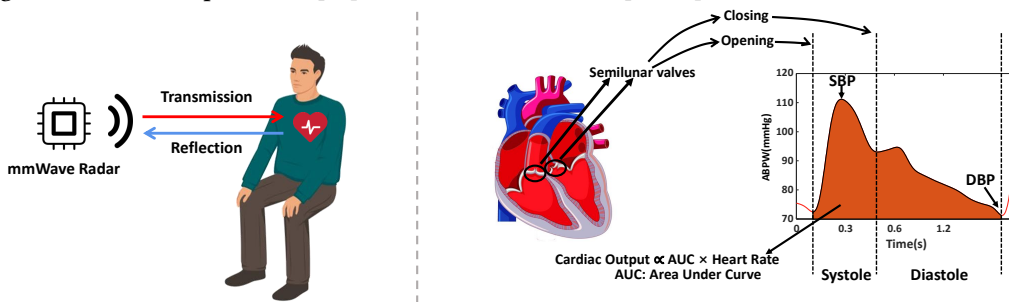


Fig. 1. Left: the typical usage scenario of monitoring AWPW with WaveBP. Right: Arterial blood pressure waveform (ABPW) depicts cardiac activities and fine-grained cardio-dynamic indicators, e.g., cardiac output. SBP and DBP are systolic blood pressure and diastolic blood pressure as the maximum and minimum values of the waveform, respectively.

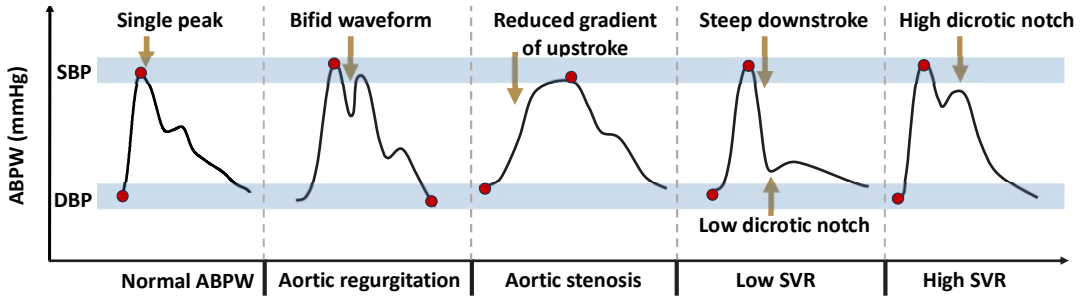


Fig. 2. Illustration of cardiac abnormalities that can be reflected in ABPW but behave similarly in discrete SBP/DBP [9]. SVR: systemic vascular resistance that is associated with the stress developed in the left ventricular during ejection [9].

non-invasive manner. However, they require either dedicated and expensive hardware (~40K USD) or close skin contact, leading to discomfort and inconvenience in daily scenarios.

To bridge this gap, we pose a question: *is it feasible to measure ABPW in a contactless manner?* With such a system, the user can just sit in front of the radar with no sensor attached, and no discomfort will arise as shown in Figure 1. To answer this question, by delving into the formation of ABPW, we examine the correlation between wireless signals reflected from the chest and ABPW with a hemodynamics Windkessel model [63] in Section 3, which regards the heart as the driver of blood circulation to characterize blood pressure variations. We observe that ABPW has a strong correlation with fine-grained cardiac activities such as heart systole and diastole, which can be captured from mmWave signals reflected from the chest. This cardiac information serves as a bridge between mmWave signals and ABPW, shedding light on the potential for contactless ABPW monitoring.

Despite this inherent association, we need to address three major challenges accordingly:

- (1) *How to map one heartbeat's mmWave reflection sequence to one heartbeat's ABPW?*
Due to the complexity of the cardiac kinetic system and the temporal inherence inside ABPW, it is hard to derive sequence-to-sequence (seq-to-seq) expressions from mmWave to ABPW to preserve the waveform details. Besides, the nature of physiological diversity across individuals makes it harder to fit into every subject.
- (2) *How to improve model robustness towards sensitive mmWave inputs under the high sampling rate requirement?*
Since ABPW relies on temporal-context analysis with a high sampling rate requirement (e.g., 125 Hz in our setting), this seq-to-seq mapping requires informative sequential mmWave inputs. However, due to the small wavelength, mmWave signals are highly sensitive to disturbances. Even millimeter-level motions may introduce large and non-linear distortions, making it challenging to acquire reliable sequential mmWave data.
- (3) *How to efficiently complement cardiac information required by ABPW to chest vibrations captured by mmWave?*
mmWave signals mainly reflect the chest vibrations caused by cardiac activities while ABPW also relates to blood volume changes in the vessels and electrical cardiac activities [14]. It is desirable but non-trivial to complement this extra information efficiently.

In this work, we propose WaveBP, a hybrid deep learning pipeline for contactless ABPW monitoring. To solve the above challenges, our design consists of three parts:

(1) **Spatial-Temporal Mapping.** We design a neural network named mmFormer with a feature extractor and a personalization module to map mmWave reflections to ABPW within the heartbeats. Previous contactless cardiac sensing works [16, 29, 65] generate cardiac signals like ECG/PPG based on the deep mmWave features with a coarse temporal resolution. Since ABPW requires a detailed temporal mapping with the whole cardiac cycle analysis (Section 3), to facilitate sequential mapping from mmWave to ABPW instead of aggregating multiple sequential mmWave reflections, we impose prior knowledge as a temporal consistency regularization that this sequential translation intends to be consistent across different temporal resolutions. The feature extractor is a hybrid Transformer [48, 58] with spatially-informed shortcuts at multiple temporal resolutions which implicitly

	WaveBP (Ours)	mmBP [52]	Kawasaki et al. [28]	Singh et al. [54]	AirBP [35]	hBP-Fi [8]	RF-BP [60]
Continuous ABPW	✓	✗	✗	✗	✗	✗	✗
Max. Distance (cm)	70	20	Nan	50	26	90	130 ¹
#subjects	43	25	3	5	41	35	70
Estimation Interval (second)	0.008	25	Nan	Nan	35	2.5	8
#BP labels per subject	1300	100	20	50	7	Nan	<100
Cover all BP categories*	✓	✗	✗	✗	✓	✗	✓
Satisfy AAMI	✓	✓	Nan	Nan	✓	✓	✓
SBP / DBP Error, (Mean ± STD, MAE)	-1.80±7.02, 5.82 0.12±5.40, 4.23	0.87±5.01, Nan 1.55±5.27, Nan	Nan, Nan Nan, Nan	Nan, Nan Nan, Nan	-0.30±4.80, 3.42 -0.23±3.79, 2.79	-2.05±6.83, Nan 1.99±6.30, Nan	0.7±6.1, 6.5 0.2±4.9, 4.7

Table 1. Compared with SOTA contactless BP estimation works, WaveBP is the first to generate accurate BP waveforms under the AAMI boundary. #: number of. Nan: not mentioned; *: BP categories are from [15]. WaveBP and RF-BP [60] sense the sitting users through the chest vibration while the others require users to fix their wrists/arms around the radar. The estimation interval indicates the required signal duration to derive one BP value.

learns ABPW sequences from spatial reflections from the subject’s chest with multi-resolution awareness. The personalization module balances the need for personalization and data collection burden with two schemes, one with no need for the user’s ABPW data and the other for sufficient ABPW data (around 20 minutes).

(2) Robustness Enhancement with Multi-View Reflections. Previous contactless discrete BP estimation works [35, 52, 60] perform data cleaning across multiple cardiac cycles to ensure performance, and thus cannot satisfy the ABPW sampling rate requirement. Different from them, we propose a beamforming-based data augmentation module (BeamDA) to enhance the model’s robustness. We observe that vital signals are distributed more consistently than noises across different beamforming angles. Based on this spatial consistency intuition, BeamDA constrains the model training to extract consistent features from different views (angles) and amplifies consistent vital sign-related information extraction with theoretically proven benefits.

(3) Knowledge Guidance from Extra Modalities. Through our analysis in Section 3, photoplethysmography (PPG) and electrocardiogram (ECG) signals are highly correlated with ABPW in values and shapes. We introduce cross-modality knowledge transfer (CMKT), a teacher-student framework that transfers the information gained from the cardiac (ECG/PPG) model to the mmWave model. The mmWave student model is co-supervised by ABPW labels and the ECG/PPG teacher model which is trained on a public dataset [34] and fine-tuned on our dataset. This process takes place in the training stage without introducing extra overhead in the testing stage.

We implement WaveBP on a commercial mmWave radar (TI IWR1443BOOST [23]) and evaluate it on a dataset of 43 subjects, including 4, 10, and 2 subjects with hypotension, hypertension stage-1 and hypertension stage-2 BP readings, respectively. The results under the leave-one-subject-out (LOSO) setting validate that our system achieves a **high waveform correlation** of 0.903 and a **low-value error** (mean ± standard deviation) of each point of (-0.14±7.48) mmHg. SBP and DBP measurements from reconstructed ABPW have low errors of (-1.80±7.02) mmHg and (0.12±5.40) mmHg, respectively, within the Association for the Advancement of Medical Instruments (AAMI) requirement (5±8) mmHg [55]. This performance could be further improved by the specialization scheme tailored for each individual and is sustainable even after a period of 6 months. To validate the real-world applicability, we conduct three case studies that show WaveBP holds great potential for fine-grained cardiac indicator estimation, cardiac abnormality detection, and continuous long-time monitoring. Our major contributions can be summarized as follows:

- We propose WaveBP, the first contactless arterial blood pressure waveform monitoring system based on a commercial mmWave radar. Specifically, WaveBP advances previous works by accurate ABPWs generation with a high sampling rate of 125 Hz for a sitting subject without any attachment.

¹RF-BP’s SBP error maintains smaller than 10 mmHg at 130 cm.

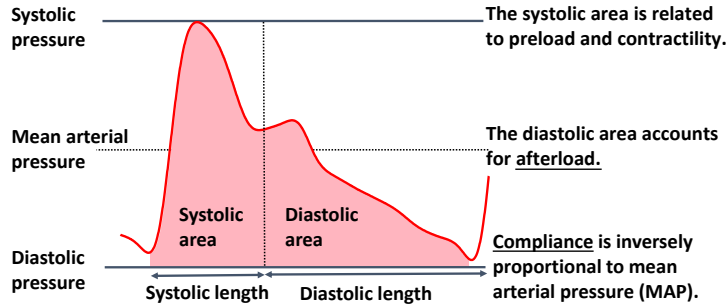


Fig. 3. An example of ABPW.

- We propose a series of techniques that overcome the challenges of mapping mmWave signals to ABPW sequences, including a hybrid Transformer model (mmFormer) with multi-resolution awareness and flexible personalization schemes, a novel radar-specific data augmentation (BeamDA) based on beamforming to focus on cardiac information across different views, and a knowledge transfer framework (CMKT) to fuse extra knowledge from cardiac modalities without extra deployment overhead.
- We conduct extensive evaluations of over 50,000 ABPW samples of 43 subjects. The results show that our system can achieve a high performance in both detailed shapes and values, and hold potential for fine-grained cardiac parameter estimation and cardiac abnormality detection. Core codes will be open-sourced².

2 PRELIMINARIES

2.1 mmWave Sensing

Basically, mmWave radar could detect the distance of surrounding reflections. It emits frequency-modulated continuous waveforms (FMCW), *i.e.*, chirps, and collects reflection signals via an antenna array. The received signals are mixed with transmitted signals to obtain intermediate frequency (IF) signals X_{IF} in the equation:

$$X_{IF}(i, t) \approx \alpha_i \exp[-j4\pi(f_c + Bt/T_c)d(t)/c], \quad (1)$$

where i denotes i -th reflection path channel. c is the light speed. α_i is the complex path loss for channel i . f_c denotes the starting frequency of chirp signals. B denotes the bandwidth of sweeping frequency. T_c denotes chirp duration. $d(t)$ denotes the distance from the sensed object, *e.g.*, the human chest to the mmWave radar. By applying Range-FFT operation [25] on the above IF signals, we can obtain the frequency and phase of IF signals:

$$f = 2Bd(t)/(cT_c), \quad \phi(t) = 4\pi d(t)/(c/f_c). \quad (2)$$

Based on the above equations, the IF signal, with a bandwidth of 4 GHz, enables object localization with a resolution of $\frac{c}{2B} \approx 4cm$. Moreover, it can detect micrometer-level distance changes through the phase $\phi(t)$ [25] and could be utilized to sense fine-grained cardiac activities [16]. We use the complex-valued representations of mmWave Range-FFT results to preserve information from both amplitude and phase aspects [73].

2.2 Arterial Blood Pressure Waveform

ABPW depicts the fluctuations in arterial blood pressure. Figure 3 exemplifies ABPW during a single cardiac cycle. In the systole stage, the left ventricle ejects blood into the aorta. The kinetic energy of the ejected blood forces the elastic aortic wall to expand, causing an increase in blood pressure. When the aortic valve closes, the previously ejected blood returns to the heart, resulting in a reduction of blood pressure [9]. The highest, lowest, and mean values of the waveform correspond to SBP, DBP, and MAP, respectively. ABPW encompasses vital

²<https://anonymous.4open.science/r/WaveBP-BBE8/>

cardiac information that holds clinical significance [9, 43, 56]. For example, the slope of the ascending waveform reflects myocardial contractility while the slope of the downstroke waveform is related to systemic vascular resistance. The systolic area and diastolic area reflect the ventricular wall stress and contractility. The cumulative area under the ABPW curve (AUC) exhibits a strong correlation with cardiac output (CO), a pivotal measure for evaluating circulatory performance and preventing heart failure [33, 56]. Figure 2 illustrates several abnormal cases of ABPW. For example, aortic regurgitation is characterized by its bifid waveform caused by abnormal blood circulation which blood pumped out of the left ventricle leaks backward. We refer interested readers to related medical references [9].

3 WAVEBP DESIGN RATIONALE

The heart is the main organ in the body circulatory system that pumps and receives blood. Heart activities introduce variations in ABPW and also cause vibrations in the human body. In this part, we would like to clarify the correlation between mmWave reflection signals and ABPW, which motivates the design of WaveBP.

As illustrated in Section 2.1, mmWave reflection signals capture fine-grained chest movements induced by heart pulsations during the systole and diastole phases. Compared with the heart pulsations captured in seismocardiogram (SCG) with an IMU sensor on the chest, Figure 4 shows that the accelerations of the mmWave phases exhibit remarkable similarity with SCG signals [16], thereby confirming the presence of detailed cardiac information within mmWave signals.

Simultaneously, the pulsations of the heart during the systole and diastole phases also lead to variations in blood flow $I(t)$ within the blood vessels, consequently causing fluctuations in blood pressure $P(t)$, i.e., ABPW. The quantitative relationship between $I(t)$ and $P(t)$ can be described by the widely utilized three-element Windkessel model in hemodynamics modeling [63]:

$$(1 + \frac{R_1}{R_2})I(t) + CR_1 \frac{dI(t)}{dt} = \frac{P(t)}{R_2} + C \frac{dP(t)}{dt}. \quad (3)$$

The two terms on the left-hand side represent the incoming blood volumes pumped from the heart and flowing out of the artery. The first term on the right-hand side represents the blood flow into the heart, while the second term represents the stored volume changes inside the artery, which can be observed through PPG signals. Besides, R_1 , R_2 and C represent individual-specific parameters, specifically denoting the aortic characteristic impedance, peripheral resistance on blood flow, and arterial compliance, respectively.

Furthermore, based on the Moens-Korteweg equation and Hughes Equation [36, 42], the initial state of $P(t)$, denoted as $P(0)$ or DBP, has a significant correlation with the pulse transit time (PTT) as demonstrated in the following equation:

$$P(0) = \frac{1}{\eta} \left[2 \ln\left(\frac{L}{PTT}\right) + \ln\left(\frac{2\rho r}{E_0 h}\right) \right]. \quad (4)$$

PTT can be approximately acquired from ECG and PPG signals [3] depicted in Figure 4. L denotes the distance of blood propagation from two measured sites. η , h , r , ρ , and E_0 are individual parameters such as the artery material coefficient, the artery thickness, the artery radius, and the elasticity modulus of the vessel wall at zero pressure, respectively.

Equation 3 and 4 illustrate the pressure value correlation while Figure 4 demonstrates the temporal correlation between ABPW and cardiac signals. Combined with the presence of detailed cardiac vibration-related information inside mmWave signals, we summarize the key insights of WaveBP as follows:

- The mutual cardiac information shared between the heart pulsations captured in mmWave reflections and ABPW serves as the primary motivation to develop a contactless mmWave-based system for estimating ABPW.

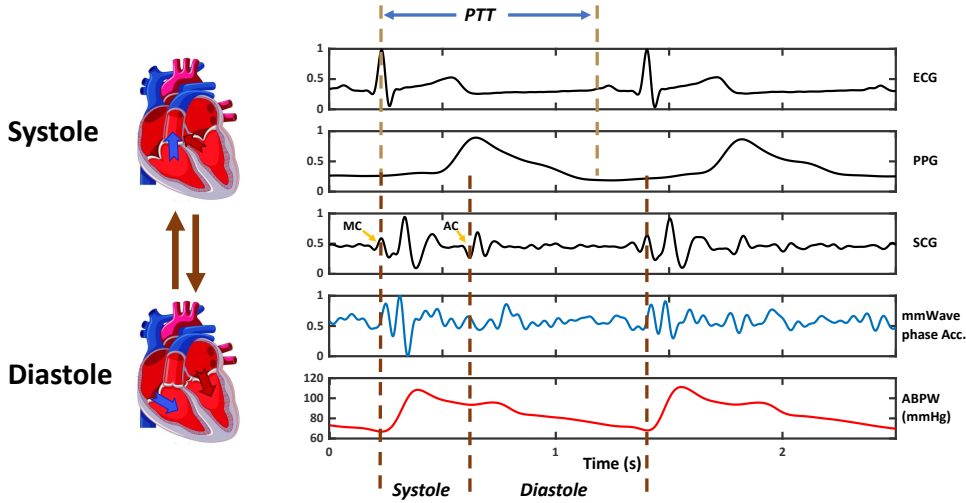


Fig. 4. Illustration of correlation among cardiac signals (ECG/PPG/SCG), mmWave signals, and ABPW, where MC refers to the closure of the mitral valve, i.e., the beginning of the systole phase, and AC denotes the closure of the aortic valve, i.e., the end of the systole phase and the beginning of the diastole phase.

ABPW requires sequential mapping and temporal-context analysis. To this end, we have designed an end-to-end deep learning model, mmFormer to effectively capture the correlations between mmWave signals and ABPW.

- Personalization is crucial as the individual parameters, such as artery thickness and blood density, vary among different subjects and can significantly impact the model as proved in Equation 3 and 4, which motivates our design on personalized regressor module as shown in Figure 7(b).
- mmWave signals are susceptible to noises, as demonstrated by the imperfect matching between mmWave phase accelerations and SCG signals in Figure 4. This motivates us to develop a robustness enhancement component, namely BeamDA to mitigate the interference.
- ABPW also relates to blood volume changes in vessels and detailed cardiac activities, which can be captured by PPG and ECG signals. It is highly desirable to fuse this information with the mechanical vibrations in mmWave signals to enhance model accuracy without imposing additional efforts on users. This motivates our design of cross-modality knowledge transfer, *i.e.*, CMKT.

4 SYSTEM OVERVIEW

WaveBP is a contactless system for monitoring ABPW using mmWave signals. As shown in Figure 5, WaveBP firstly collects multi-channel mmWave reflections with Range-FFT demodulation from the subject's chest. The extracted data is then fed to the core components of WaveBP, which consist of mmFormer as the deep learning model, Beamforming-based Data Augmentation (BeamDA), and Cross Modality Knowledge Transfer (CMKT).

mmFormer comprises a feature extractor and a personalized waveform regressor. The feature extractor utilizes a hybrid Transformer architecture [48, 58] with spatially-informed shortcuts. Enhanced by the UNet architecture, mmFormer is featured with multi-resolution awareness for effective temporal mapping. As discussed in Section 3, the regressor accounts for personalization as a practical consideration. We have designed two schemes to address different levels of personalization efforts.

The BeamDA module employs beamforming techniques to convert raw signals into a batch of samples with varying beamforming angles to train mmFormer. The underlying rationale is that cardiac signals, which are highly correlated with ABPW, tend to exhibit greater consistency across different angles compared to noise

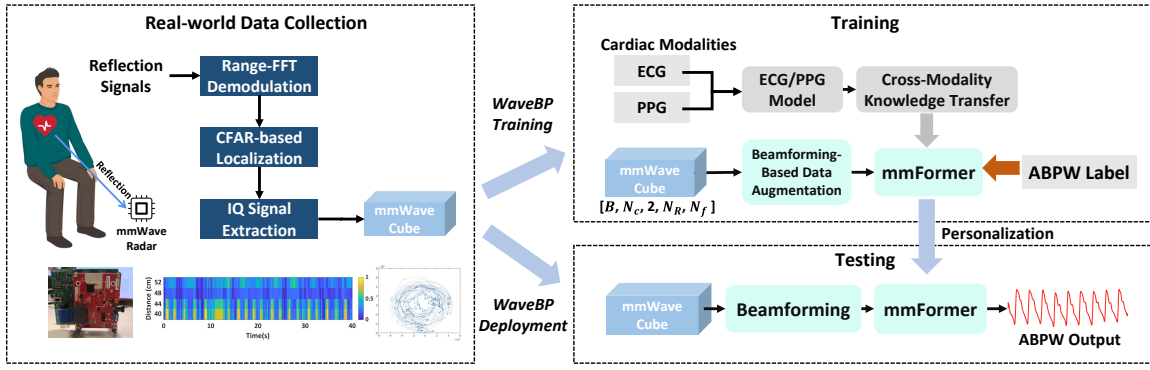


Fig. 5. Overview of WaveBP.

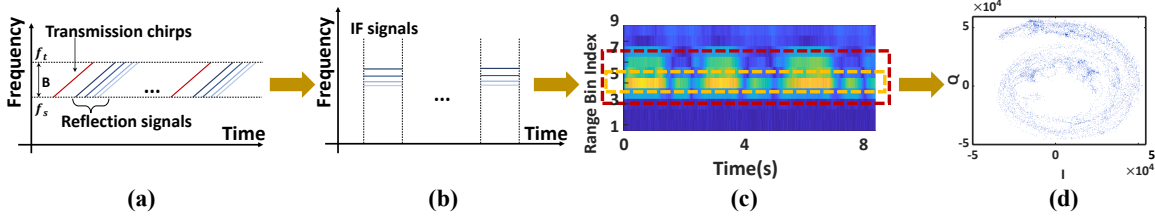


Fig. 6. Data collection process. (a). Transmission and reflection signals; (b). Intermediate frequency signals; (c). Range-FFT operations; (d). Complex-valued IQ signal extraction.

signals. The augmented data $\tilde{X}(\theta)$ for target angles θ are fed into the model separately for training to enforce the consistency regularization across the angles.

The CMKT module facilitates the transfer of learned knowledge from an ECG/PPG-ABPW teacher model to mmFormer. The teacher model supervises mmFormer to extract cardiac-related features that are relevant to ABPW estimation. This ensures that mmFormer captures the essential information from the mmWave signals that correlate with cardiac activity. ECG/PPG signals are only utilized in the training phase, *i.e.*, no additional overhead is introduced during deployment. Additionally, mmFormer is also supervised using ABPW labels, which guide the model to regress ABPW values accurately.

As the enhancement of mmFormer's training scheme, BeamDA and CMKT are only employed in training. During the testing phase, we apply the beamforming algorithm [16] to the mmWave signals and feed the beamformed signals into mmFormer for ABPW estimation.

5 SYSTEM DESIGN

5.1 Data Collection

As illustrated in Section 2.1, WaveBP employs a commercial radar to transmit FMCW chirps (Figure 6(a)) and generate IF signals (Figure 6(b)). The distance information inside IF signals can be revealed with Range-FFT operation [25] (Figure 6(c)). Furthermore, we use the Constant False Alarm Rate (CFAR) detection algorithm [46] to locate the potential region of the human chest and then search the range bin with the largest reflection energy as shown in the yellow dashed area in Figure 6(c). Inspired by existing practice [73], we extract multiple adjacent reflection bins as the input data $X \in \mathbb{R}^{N_c \times 2 \times N_b \times N_f}$. Here, N_c , N_b , and N_f are the number of wireless channels between the transmitting and receiving antennas, the number of selected bins in Range-FFT results and

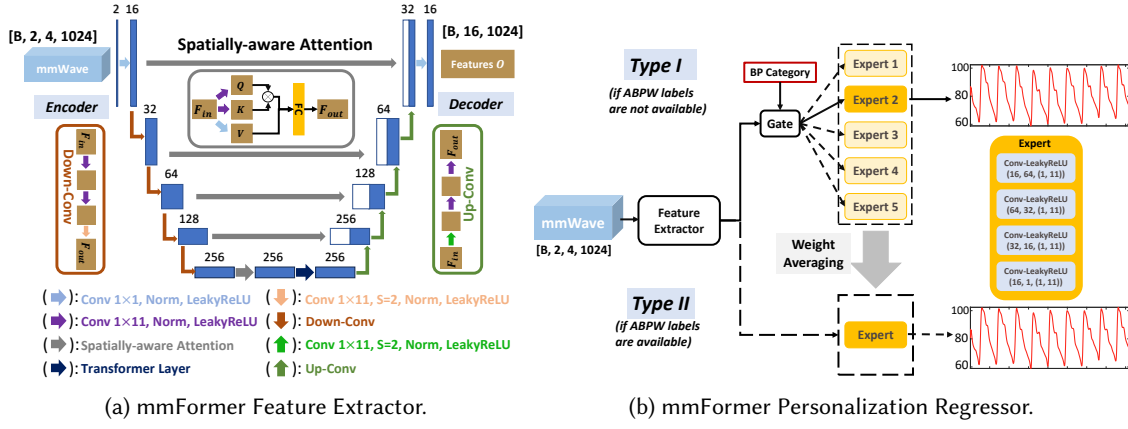


Fig. 7. The architecture of mmFormer.

the number of frames, respectively, and the number of 2 represents the real and imaginary parts of the complex signals. Figure 6(d) is an example of complex-valued mmWave data extracted from one range bin.

5.2 mmFormer Architecture

mmFormer includes two components: a hybrid Transformer feature extractor with multi-resolution awareness and spatially-aware shortcuts, and a personalization module for flexible adaptation.

5.2.1 Hybrid Transformer-based Feature Extractor. To derive beat-to-beat relations from mmWave signals reflected by cardiac activities to corresponding ABPWs, we formulate this problem as a time series mapping task. A reliable mapping intends to be consistent across different temporal resolutions.

Based on this temporal consistency regularization, we design the mmFormer feature extractor with multiple resolutions. To aggregate the features from multi-resolution layers, we leverage the UNet architecture [48] with spatially-informed shortcuts to preserve discriminative features from the same resolution. In Figure 7(a), the left part focuses on encoding mmWave signals using convolution operations with 5 blocks corresponding to different time resolutions. Each layer encodes the mmWave signals and downsamples them for the subsequent layer with the convolution kernels with a stride of $S = 2$. The final layer, with the largest receptive field, is enhanced with Transformer layers [58] to leverage their superior capability in modeling time series relationships. The right side of the backbone involves upsampling the downsampled embeddings from the lower layers using transposed convolution kernels and combining them with the passed representations from the encoder at the same layer.

5.2.2 Spatially-Aware Attention as Shortcuts. In mmFormer, shortcuts from the encoder to the decoder are crucial to concatenate feature maps to avoid information loss at different scales. Different from typical UNet models [48] that both the input and the output share the same dimension, the shortcuts in mmFormer should aggregate multiple mmWave reflections from the human chest to derive the target ABPW features.

To this end, we integrate an attention module as the spatially-informed shortcuts to ensure its effectiveness across different chest dynamics. Figure 8 depicts two mmWave reflection signals with varying reflection distributions, which can be attributed to the different breathing patterns adopted by the subjects. In the scenario depicted in Figure 8(a), where the chest is closer to the radar than the diaphragmatic region, we observe that during chest breathing (Figure 8(b)), a higher concentration of reflection energies is observed in the bins near the radar, whereas during diaphragmatic breathing (Figure 8(c)), the energy is more focused on the bins farther away from the radar. Thus, we introduce an attention mechanism to make the model dynamically aggregate the signals. Specifically, given the features extracted from multiple reflection signals as $F_{in} \in \mathbb{R}^{D \times N_b \times T}$, where D

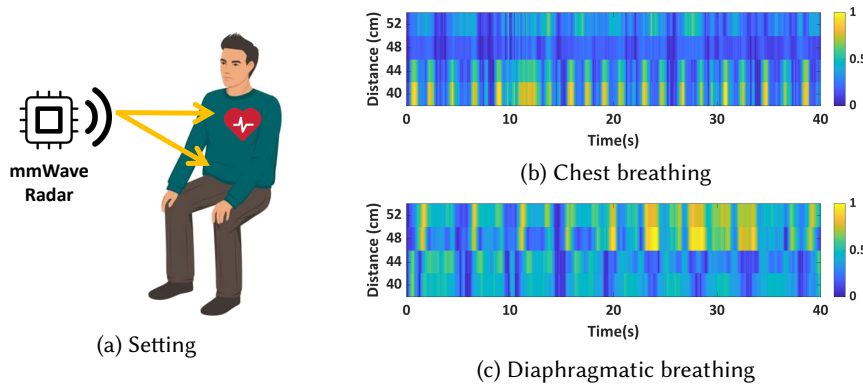


Fig. 8. Different reflection signal distributions caused by breathing patterns.

represents the dimension of feature channels, N_b represents the number of reflected areas, and T represents the time length of the sequence, the aggregated result F_{out} can be calculated:

$$\begin{aligned} Q &= f(\text{Conv}_Q(F_{\text{in}})), K = f(\text{Conv}_K(F_{\text{in}})), V = f(\text{Conv}_V(F_{\text{in}})) \\ C &= \text{Softmax}\left(\frac{QK^T}{\sqrt{D}}\right), \quad F_{\text{out}} = FC(CV), \end{aligned} \quad (5)$$

where Q , K , and V represent the calculated query, key, and value in the attention module, respectively. Conv_i denotes the convolution operator for $i \in \{Q, K, V\}$, and f represents the non-linear activation function. The matrix $C \in \mathbb{R}^{D \times N_b \times N_b}$ is the learned correlation matrix, which indicates the importance of signals from different reflection areas. Finally, FC refers to the fully-connected layer that projects the weighted value V from N_b to 1. As shown in Figure 7(a), we incorporate this attention module into each layer of mmFormer to facilitate information delivery from the encoder's perspective to the decoder. Figure 9 is an example of feature visualization from the mmFormer feature extractor. The generated feature map has 16 channels, while the lighter color indicates a larger value in the feature map. We can observe that the learned features from the end-to-end neural network are in good agreement with the ground truth in terms of time and amplitude aspects. From the time aspect, the overall pattern in the feature map corresponds well to each cycle of the waveform, indicating good cardiac cycle feature extraction. From the amplitude aspect, the largest value in the feature map occurs in the trough of the ABPW, which indicates the features capture the amplitude derivatives of ABPW.

5.2.3 Practical Considerations. Our analysis indicates that individual parameters are crucial in the mmWave-ABPW model, as demonstrated by Equations 3 and 4. Previous assessments [10, 50, 51] also verify that PPG-based ABPW estimation methods suffer from data distribution shifts caused by the inherent diversity of physiological structures, which greatly influences the performance of inter-subject estimation. In our preliminary study on a large public ABPW dataset MIMIC II [34] shown in Table 2, the current leading ECG/PPG-based ABPW monitoring method, V-Net [17], has an unsatisfactory performance under inter-subject testing without knowing the discrete blood pressure values for personalization. Since acquiring personal parameters such as blood density is challenging, we resort to data-driven calibrations. To address the practical issue of data collection burdens, we have designed two schemes depicted in Figure 7(b).

Type I is designed for the scenario where the user's ABPW labels are unavailable due to the high cost of ABPW collection devices. In this scheme, we design different expert regressors with an explicit gate on BP categories following the classification by the American Heart Association [15], *i.e.*, five BP categories, hypotension, normal, elevated, hypertension stage-1, and hypertension stage-2. In the training phase, the feature extractor learns the

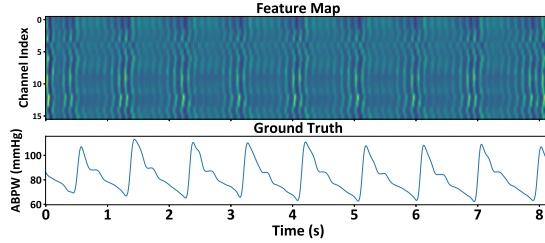


Fig. 9. Example of extracted features.

representations for every input and then forwards them to the corresponding category expert. In the testing phase, our model only requires knowledge of the coarse BP category, *e.g.*, obtained using a low-cost cuff-based BP monitor, and selects the appropriate regressor for ABPW estimation without tuning the model weights.

Type II is designed for scenarios where the user's ABPW data is available. It builds upon the general model trained with different BP categories from **Type I**. In this case, we only have one expert regressor initialized with weight averaging on the five experts learned from the **Type I** model. After initialization, the **Type II** model undergoes further training using the user's ABPW data to personalize the model. The personalized model captures individual characteristics to eliminate the need for BP category input during inference.

5.3 BeamDA Scheme

We propose BeamDA with theoretical analysis to help learn informative features from noisy mmWave signals. Instead of relying solely on large dataset collection or traditional noise elimination techniques, we adopt a data augmentation perspective to increase the number of samples while simultaneously improving the data quality.

We basically utilize the beamforming technique to enhance mmWave signals, which involves combining different mmWave propagation paths to focus on the target direction. For a beamforming angle θ , we can represent the beamforming signal as follows:

$$\tilde{\mathbf{X}}(\theta) = \mathbf{W}^H(\theta)\mathbf{X}, \quad (6)$$

where $\mathbf{W}(\theta) = [W_1(\theta), W_2(\theta), \dots, W_{N_c}(\theta)]$ represents the steering vector of angle θ computed as:

$$W_c(\theta) = \exp[-j2\pi d_c \sin(\theta)/\lambda], \quad (7)$$

where λ is the wavelength of the mmWave and d_c is the relative distance introduced by the channel c . The BeamDA scheme utilizes beamforming to generate a batch of signals with varying beamforming angles. Thus, we can obtain multiple views of the target for data augmentation.

5.3.1 Empirical Illustration. To illustrate BeamDA's rationale, we conducted a case study where a subject sat in front of the radar. We measured the vital signs from two different beamforming angles that maximized the signal strength of the heartbeat frequency bands [16] and the received power, which were set at 30° and 0° , respectively. The beamforming results of Barlett beamformer [4] are shown in Figure 10. From Figure 10(d) to Figure 10(f), the signal phases are influenced by noise to varying extents. However, the overall waveforms induced by breaths (*e.g.*, large cycles) and heartbeats (*e.g.*, peaks) are still preserved. This indicates that noise distributions, such as tremors or unconscious movements of users in different locations, may exhibit differently in different views (angles) of the mmWave signals. While vital signs, such as breaths and heartbeats, tend to be more consistent.

5.3.2 Algorithm Design. Based on this observation, we have devised the BeamDA scheme, outlined in Algorithm 1. In the training stage, we apply beamforming using Equation 6 and 7 to the training data with random angles. Additionally, we include signals from one antenna without beamforming to preserve essential information. I/Q data in Figure 10(a) and 10(b) can be regarded as augmented examples of the non-beamforming one in Figure

Model	Personalization	ME (mmHg)		STD (mmHg)	
		SBP	DBP	SBP	DBP
V-Net	No	5.34	-11.2	18.44	21.45
V-Net	Type I	1.66	-1.93	14.62	7.75
Ours	Type I	1.22	1.23	12.34	6.95

Table 2. Inter-subject test on MIMIC II (ECG/PPG).

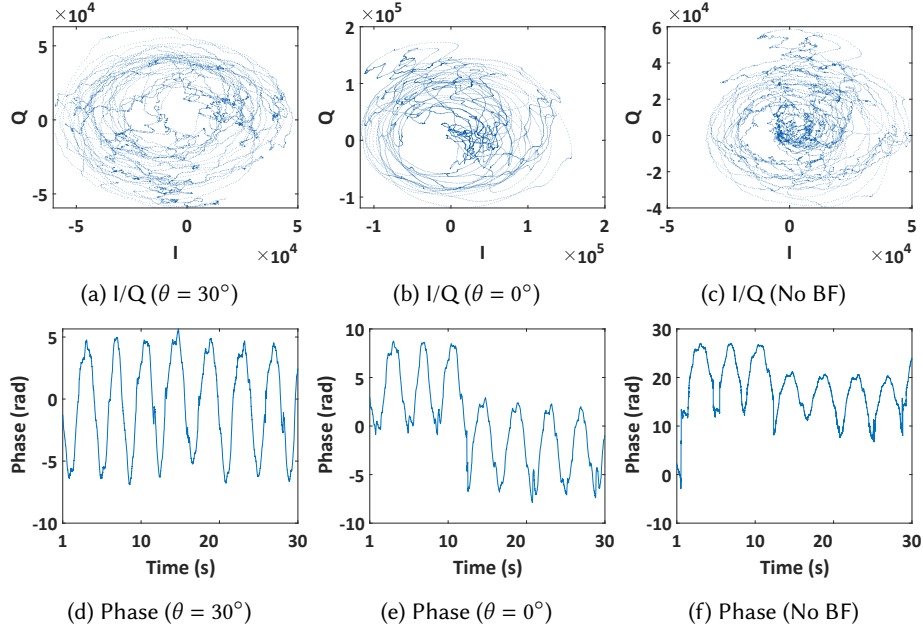


Fig. 10. Illustration of different beamforming angles.

10(c). The training loss is calculated averagely on the augmented inputs on the same ground truth based on the intuition that observations from different views should produce the same results. By training on signals from multiple beamforming angles, the model can effectively retain common cardiac information while mitigating noise and variations effects. In the testing phase, we employ the beamforming algorithm [16] to generate signals that focus on the heart area. Subsequently, we feed them to our model, mmFormer, for further estimation.

5.3.3 Theoretical Insight. To substantiate the effectiveness of BeamDA, we analyze the empirical risk on augmented samples with the following equation:

$$\begin{aligned} \xi^{\text{BeamDA}}(\mathcal{F}) &= \mathbb{E}_{\theta} \left[l \left(\frac{1}{N_{\text{aug}}} \sum_{i=0}^{N_{\text{aug}}-1} \left| \left| \sum_{j=0}^{N_c} W^H(\theta_j) / N_c \right| \right| y, \frac{1}{N_{\text{aug}}} \mathcal{F} \left(\sum_{j=0}^{N_c} W^H(\theta_j) X_j \right) \right) \right], \\ &= \mathbb{E}_{\theta} \left[l \left(\frac{1}{N_{\text{aug}}} \sum_{j=0}^{N_c} |\lambda_j| \tilde{y}, \frac{1}{N_{\text{aug}}} \mathcal{F} \left(\sum_{j=0}^{N_c} \lambda_j X_j \right) \right) \right], \text{ where } \tilde{y} = \frac{N_{\text{aug}}}{N_c} y, \lambda_j = W^H(\theta_j). \end{aligned} \quad (8)$$

In Equation 8, $\xi^{\text{BeamDA}}(\mathcal{F})$ is the empirical risk after BeamDA. \mathcal{F} stands for the model to train, *i.e.* mmFormer. \mathbb{E}_{θ} is the expectation function on the random-sampled beamforming angles. X_j is the mmWave data from the channel index j while y is the ABPW label. $l(\cdot, \cdot)$ is the calculated loss where the first item stands for the label while the second is the input. Note that we use the same ABPW label y for the same mmWave inputs X_j with different angles and derive the loss with averaging losses from the augmented samples. We could observe that after BeamDA, the empirical risk is a specialized mix-up form [69] that combines inputs from multiple antennas with beamforming weights λ_j . This mix-up loss has been theoretically proved effective in training that helps improve robustness and generalization [70].

Algorithm 1 Beamforming-based Data Augmentation

Input: A minibatch of multi-channel mmWave data \mathbf{X} , number of channels N_c , the relative channel distance list $[d_0, d_1, \dots, d_{N_c-1}]$, number of augmented samples N_{aug} , starting Angle θ_s , ending angle θ_e

- 1: **for** $0 \leq i < N_{aug}$ **do**
- 2: $\theta_i \leftarrow$ Random sample from $[\theta_s, \theta_e]$
- 3: **for** $0 \leq c < N_c$ **do**
- 4: $W_c(\theta_i) = \exp\left[\frac{-j2\pi d_c \sin(\theta_i)}{\lambda}\right]$
- 5: **end for**
- 6: $\mathbf{W}(\theta_i) = [W_0(\theta_i), W_1(\theta_i), \dots, W_{N_c}(\theta_i)]$
- 7: $\tilde{\mathbf{X}}(\theta_i) = \mathbf{W}^H(\theta_i)\mathbf{X}$
- 8: **end for**

Output: $[\tilde{\mathbf{X}}(\theta_0), \tilde{\mathbf{X}}(\theta_1), \dots, \tilde{\mathbf{X}}(\theta_{N_{aug}})]$

5.4 Cross Modality Knowledge Transfer

As illustrated in Section 3, ABPW highly relates to blood volume changes in vessel information and detailed cardiac activities embedded in PPG and ECG signals, respectively. It is better but non-trivial to embed extra knowledge of ECG/PPG into the mmWave-based ABPW model to enhance performance efficiently. Instead of directly feeding ECG/PPG signals into the model, we want to fuse ECG-PPG signals with no extra deployment burden. Therefore, we introduce cross-modality knowledge transfer (CMKT) as shown in Figure 11, *i.e.*, a teacher-student framework. In the training stage, we obtain an ECG-PPG teacher model from other sources and align it with our collection. Its knowledge from intermediate layers is then transferred to the student mmWave model as a regularization to enforce ECG-PPG related feature extraction. In the testing stage, the mmWave model can work without the ECG-PPG teacher model.

Teacher: The ECG/PPG-ABPW Model. The ECG/PPG-ABPW model's architecture is similar as mmFormer, but the teacher model doesn't require spatially-aware attention as shortcuts to aggregate the encoder's information. We concatenate the ECG/PPG signals in the channel dimension and feed them to our teacher model. To enhance the teacher model's capability, we firstly pre-train the teacher model in a cleaned version of MIMICII dataset [27, 34] which was collected in the intensive care unit scenarios for 942 patients. Then, we transfer the pre-trained model to our dataset by finetuning the first 1×1 convolution kernel, the first layer of the UNet architecture's encoder and decoder, and normalization parameters of the transformer layers since they contain most domain-specific features [53, 66]. All other parameters are frozen. To minimize the error of estimation results, we use the following loss function \mathcal{L}_w which combines the point estimation and the correlation of the whole waveform:

$$\mathcal{L}_2(\hat{y}, y) = \|\hat{y} - y\|^2 \quad (9)$$

$$\mathcal{L}_c(\hat{y}, y) = \frac{\sum_i (\hat{y}^i - \mu_{\hat{y}})(y^i - \mu_y)}{\sqrt{\sum_i (\hat{y}^i - \mu_{\hat{y}})^2 \sum_i ((y^i - \mu_y)^2)}}, \quad (10)$$

$$\mathcal{L}_w(\hat{y}, y) = \alpha * \mathcal{L}_2(\hat{y}, y) + \beta * \mathcal{L}_c(\hat{y}, y), \quad (11)$$

where α and β are hyperparameters to balance the loss components, \hat{y} and y are the estimation and label, $\mu_{\hat{y}}$ and μ_y are the mean values of \hat{y} and y , \hat{y}^i and y^i are the i -th point in the estimated and label waveforms, respectively.

Student: The mmWave Model. The student mmWave-model's architecture is mmFormer, as mentioned in Section 5.2. During training, it first performs BeamDA to generate diverse input samples. To transfer knowledge from the ECG/PPG-ABPW model to the mmWave model, for each input sample, mmFormer optimizes towards minimal distance between the estimation and the label as well as minimal distance between the mmWave model's

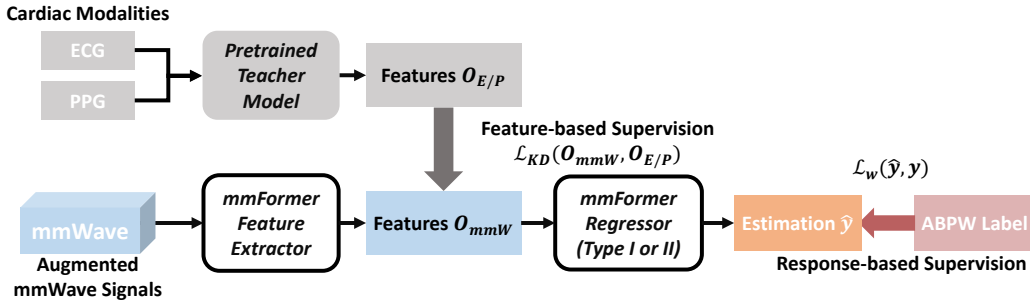


Fig. 11. Framework of cross-modality knowledge transfer.

extracted features and the ECG/PPG-ABPW model's features [47]. The loss function \mathcal{L} for the mmWave model is:

$$\mathcal{L}_{KD}(O_{mmW}, O_{E/P}) = ||O_{mmW} - O_{E/P}||^2, \quad (12)$$

$$\mathcal{L}(\hat{y}, y, O_{mmW}, O_{E/P}) = \alpha * \mathcal{L}_2(\hat{y}, y) + \beta * \mathcal{L}_c(\hat{y}, y) + \gamma * \mathcal{L}_{KD}(O_{mmW}, O_{E/P}), \quad (13)$$

where O_{mmW} and $O_{E/P}$ are the extracted features from the mmWave model and teacher model as shown in Figure 11. In our setting, we select the extracted features from the output of the mmFormer feature extractor, *i.e.*, the first layer of the UNet-based mmWave model and ECG/PPG-ABPW model decoders as O_{mmW} and $O_{E/P}$, respectively.

In summary, CMKT has the following advantages: 1). It requires ECG-PPG signals only during training and eases the requirement for input data. 2). It does not require the teacher model and student model to be the same, which brings more flexibility. Besides, since the teacher model can be pre-trained through public datasets, this method can implicitly enhance the student model's capability with a stronger teacher model.

6 IMPLEMENTATION

Sensing Platform. We implement WaveBP with a COTS mmWave radar, TI IWR1443BOOST board [23] with a TI DCA1000EVM board [22] to acquire raw data as shown in Figure 12. The radar operates on the 77 GHz with a bandwidth of 4 GHz. This radar contains 3 transmitting antennas and 4 receiving antennas. We let the radar transmit signals with two transmitting antennas simultaneously for higher transmission power and receive signals by four receiving antennas. The mmWave device sends one frame for every $T_f = 0.002$ s. We use one chirp in each frame with 256 sampling points.

Ground Truth Platform. The ABPW ground truth is collected by an FDA-approved continuous blood pressure waveform monitoring device, CNAP Monitor 100D [20], which is synchronized with an ECG sensor and a PPG sensor by the BIOPAC MP160 system [19].

Platform Synchronization. We attach another ECG sensor [18] synchronized with the mmWave radar with ADS1299EEGFE [21] through the hardware trigger. The time delay between our sensing platform and ground truth platform is calibrated by minimizing the time offsets of the extracted R peaks from the two ECG sensors.

Data Collection. We collect a dataset to implement and evaluate WaveBP with the IRB approval of our institute. We recruited 43 volunteers (20 females and 23 males) including 4 with hypotension, 24 with normal, 3 with elevated, 10 with hypertension stage-1, and 2 with hypertension stage-2 ABPW readings, respectively. All participants self-reported no cardiac disease. Since the medical reference [20] fails due to ABPW intrinsic variations in response to body motions, our data does not consider large motions currently. Following the standard validation procedure [55], the subjects were asked to wear daily attire, sit with support, and keep legs uncrossed, with the requirement that the cuff-based ground truth collection is not influenced. They are seated in a chair around 30 cm from the mmWave radar positioned in front of their chests. We conducted over 400 experimental trials on different days, each lasting around 3-5 minutes. There is a 10-minute break between each session. In each trial, subjects are asked to breathe normally in their comfortable postures and avoid large motions (*e.g.*, moving arms).

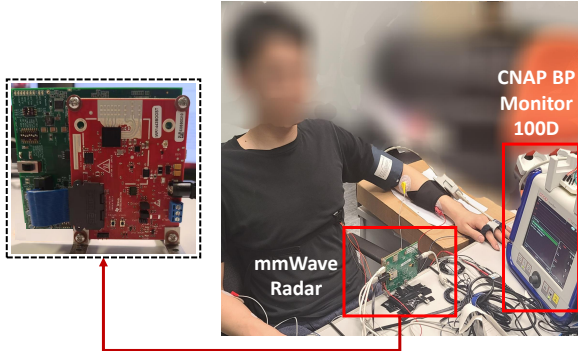


Fig. 12. Experimental environment.

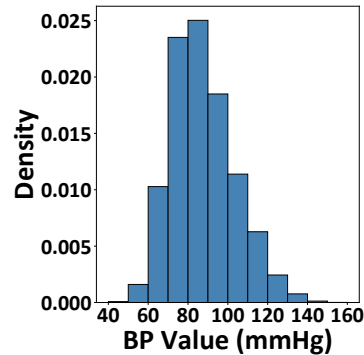


Fig. 13. Point-level BP distribution.

To mitigate the white-coat effect [15], the screen of the BP monitor is invisible to the subjects. A small portion of samples was excluded due to device instability. In total, we collect over 50,000 ABPWs, each corresponding to one heartbeat. The ABPW points have a wide distribution from 41 to 156 mmHg as summarized in Figure 13.

Software. We implement WaveBP with one NVIDIA RTX 3090 GPU based on PyTorch 1.11.0. The ECG/PPG teacher model is firstly pre-trained on a cleaned MIMICII dataset [27] containing ECG, PPG and ABPW with the preprocessing techniques in [37] and then transferred to our dataset with a batch size of 128 and learning rate of $1e^{-4}$ in 10 epochs. We downsample our sampling rate from 500 Hz to 125 Hz to align with the sampling frequency of MIMICII. The size of the mmWave data $X \in \mathbb{R}^{N_c \times 2 \times N_b \times N_f}$ before BeamDA is set as $N_c = 4$, $N_b = 4$, and $N_f = 1024$. We use the sliding window of 128 along the slow time axis to create the training samples. The ECG/PPG teacher model, the mmWave Type I model, and the personalized Type II model have initial learning rates of $1e^{-3}$, $2e^{-4}$ and $5e^{-5}$, respectively. All learning rates decay in a cosine manner to its $1/20$ in 25 epochs. We train the models with the Adam optimizer and a batch size of 64. For the BeamDA module, we augment the mmWave signals by randomly selecting 4 angles within -60° and 60° with a step of 10° considering the radar's angular resolution. The number of input channels, output channels, and kernel size of the first IQ-convolution kernel to fuse I/Q data on the first layer is 2, 16, and (1, 1). All other convolution kernels have a kernel size of (1, 11). The numbers of output channels of UNet-convolution kernels, Downsample-convolution kernels, and spatially-aware attention modules of mmFormer's encoder are 16, 32, 64, and 128, respectively. The last layer contains a convolution kernel with 256 output channels, followed by transformer layers. The number of the transformer layer is 12 and each layer has 8 heads. The numbers of output channels of UNet-convolution kernels and Upsample-convolution kernels of mmFormer's decoder are 128, 64, 32, and 16, respectively. The numbers of output channels of each regressor's convolution kernels are 64, 32, 16, 1. All the normalization modules are InstanceNorm. All the nonlinear activation functions are LeakyReLU with a negative slope of 0.3. For the loss function, we empirically set the loss weight parameters as $\alpha = 1$, $\beta = 100$, $\gamma = 50$.

7 EVALUATION

7.1 Evaluation Methodology

We will evaluate **Type I** and **Type II** schemes separately to fully assess the performance of WaveBP .

For the **Type I** scheme, we use a leave-one-subject-out (LOSO) setup to evaluate WaveBP , which involves splitting the 43-subject dataset into two parts: one contains 42 subjects for training and the other contains one subject for testing. In the Type I scheme, the model is only aware of the test subject's coarse BP category for testing rather than the detailed ABPW data. This setup assesses the model's ability to generalize to unseen subjects and is more applicable to real-world scenarios.

Level	Point	Statistic	Waveform
Metric Formula	$ME_p = \frac{\sum_{i=1}^M (\hat{p}_i - p_i)}{M}$	$ME_s = \frac{\sum_{k=1}^N (\hat{v}_k - v_k)}{N}$	
	$STD_p = \sqrt{\frac{\sum_{i=1}^M (\hat{p}_i - p_i - ME_p)^2}{M}}$	$STD_s = \sqrt{\frac{\sum_{k=1}^N (\hat{v}_k - v_k - ME_s)^2}{N}}$	$PCC_w = \frac{\sum_{j=1}^L (\hat{y}^j - \mu_{\hat{y}})(y^j - \mu_y)}{\sqrt{\sum_{j=1}^L (\hat{y}^j - \mu_{\hat{y}})^2 \sum_{j=1}^L ((y^j - \mu_y)^2)}$
	$MAE_p = \frac{\sum_{i=1}^M (\hat{p}_i - p_i) }{M}$	$PCC_s = \frac{\sum_{k=1}^N (\hat{v}_k - \mu_{\hat{v}})(v_k - \mu_v)}{\sqrt{\sum_{k=1}^N (\hat{v}_k - \mu_{\hat{v}})^2 \sum_{k=1}^N ((v_k - \mu_v)^2)}}$	

Table 3. Evaluation metrics. Here, L is the length of the waveform, N is the total number of waveforms, $M = N \times L$ is the total number of blood pressure points, and the mean values of \hat{y}, y, \hat{v}, v are $\mu_{\hat{y}}, \mu_y, \mu_{\hat{v}}, \mu_v$, respectively.

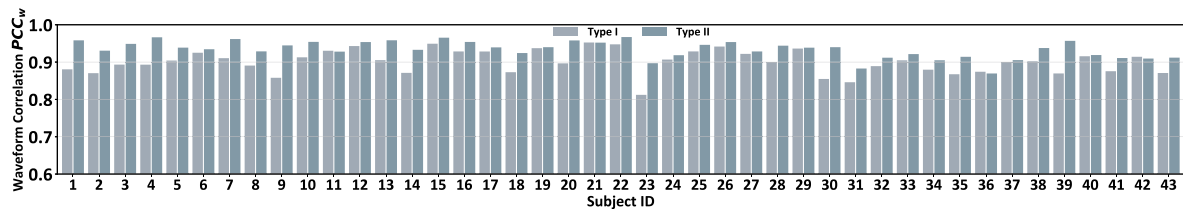


Fig. 14. Estimated waveform correlation for each subject.

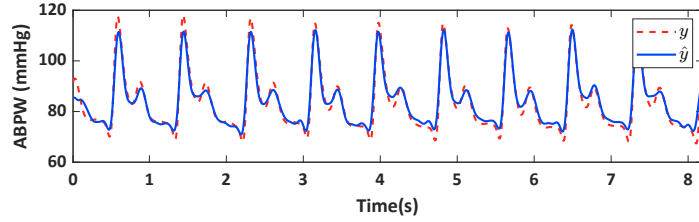
For the **Type II** scheme, we personalize the basic model from Type I with the target user's data. To avoid samples with adjacent timesteps split into train/test sets, we retrain the model acquired from the Type I scheme with the random 70% of collected trials and then test its performance for the other 30% trials. The average number of samples for each subject is 866 (train) and 435 (test).

To measure WaveBP's performance, we employ three levels of evaluation metrics as shown in Table 3. The first level assesses point estimation, including mean error (ME_p), standard deviation (STD_p), and mean absolute error (MAE_p). The second level uses the Pearson Correlation Coefficient (PCC_w) to compare the estimated waveforms with the references. For the third level, we choose the commonly used mean error (ME_s), the standard deviation of the error (STD_s), and Pearson Correlation Coefficient (PCC_s) of the discrete BP values, i.e., SBP and DBP.

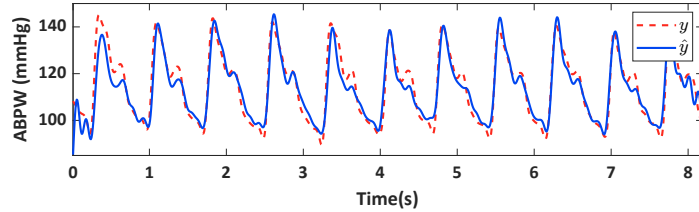
7.2 Overall Performance

7.2.1 Evaluation at Waveform Level. We will first discuss WaveBP's performance in waveform estimation. We present waveform correlations for each individual as shown in Figure 14. Both schemes have high waveform correlations for these individuals: The average PCC_w for all samples are 0.903 (Type I) and 0.935 (Type II), while the lowest and the highest PCC_w are 0.812 and 0.952 (Type I), 0.869 and 0.967 (Type II), respectively.

Figure 15 displays two examples of the estimated ABPW \hat{y} and reference values y . Figure 15(a) shows an example from a subject with normal blood pressure estimated with the Type II scheme, while Figure 15(b) is from a subject in hypertension stage 1 estimated from the Type I scheme. We can observe that WaveBP accurately tracks the changes in blood pressure waveforms for most of the middle area, while errors are larger at the beginning and end of the waveforms. This is because the attention modules of our mmFormer extract features based on the correlation between one point and its neighbors. However, for the beginning and end points, there are fewer neighbors to help calculate attention, thus resulting in poor performance. This problem can be solved from two aspects: (1) we can extend the input duration since our model can accommodate inputs with any length thanks to the convolution kernels and transformer layers; (2) we can use a sliding window to generate more reliable middle-area ABPW to replace the prediction of ending points.



(a) An example of a normal subject.



(b) An example of a Hypertension Stage 1 subject.

Fig. 15. Two examples of WaveBP. (a) and (b) are outputs from WaveBP Type II and Type I, respectively. y is the ground truth and \hat{y} is WaveBP's estimation.

	AAMI			WaveBP (Type I)			WaveBP (Type II)			RF-BP [60]		
BP Type	SBP	DBP	Point-level	SBP	DBP	Point-level	SBP	DBP	Point-level	SBP	DBP	
ME	≤ 5	≤ 5	-0.14	-1.80	0.12	-0.62	-1.54	-0.50	-	0.7	0.2	
STD	≤ 8	≤ 8	7.48	7.02	5.40	6.54	6.80	5.47	-	6.1	4.9	
MAE	-	-	5.70	5.82	4.23	4.99	5.43	4.21	-	6.5	4.7	

Table 4. Performance of point- and statistic- level metrics ($ME \pm STD$ and MAE in mmHg).

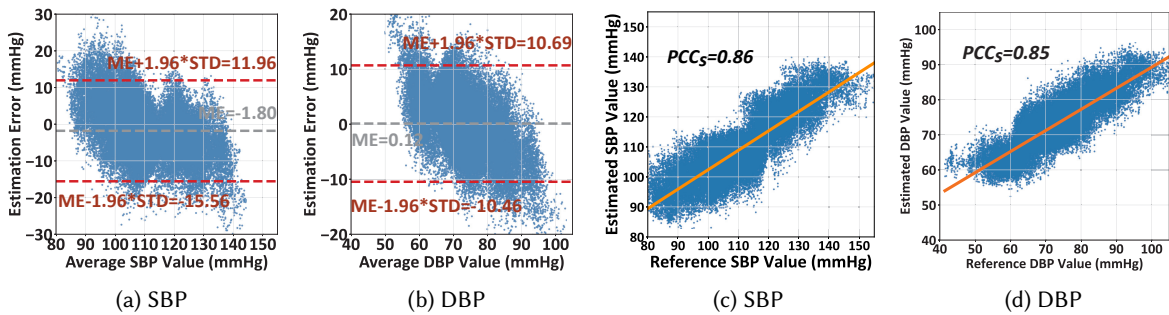


Fig. 16. (a)-(b): Bland-Altman diagram of Type I; (c)-(d): Correlation diagram of WaveBP (Type I).

7.2.2 Evaluation at Point and Statistic Levels. We present an evaluation of WaveBP at point- and statistic- level metrics. All the value-based (point-level, SBP, and DBP from statistic-level) errors meet the requirements of AAMI [55] shown in Table 4. **Point-level:** Both personalization schemes produce low measurement errors ($ME_p \pm STD_p$) and MAE_p , with Type I achieving (-0.14 ± 7.48) mmHg and 5.70 mmHg, and Type II achieving (-0.62 ± 6.54) mmHg and 4.99 mmHg, respectively. Due to the subject-specific personalization scheme, Type II will perform better than Type I as expected. **Statistic-level:** The statistic evaluations provide discrete SBP and DBP

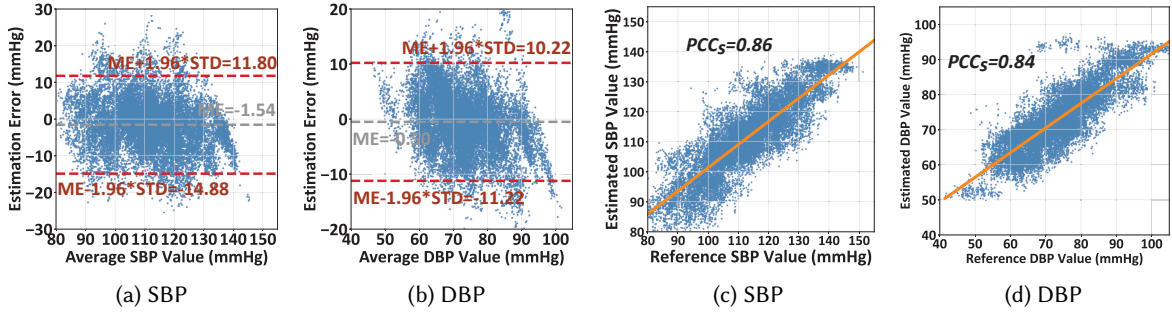


Fig. 17. (a)-(b): Bland-Altman diagram of Type II; (c)-(d): Correlation diagram of WaveBP (Type II).

	WaveBP (Type I)			WaveBP (Type II)			Crisp-BP [7]			V-Net [17]			WaveBP (teacher)		
BP Type	Point	SBP	DBP	Point	SBP	DBP	Point	SBP	DBP	Point	SBP	DBP	Point	SBP	DBP
ME	-0.14	-1.80	0.12	-0.62	-1.54	-0.50	-	1.67	0.86	-0.08	0.55	-0.79	0.02	-1.73	0.26
STD	7.48	7.02	5.40	6.54	6.80	5.47	-	7.31	6.55	7.82	7.86	5.94	6.54	6.93	4.64
MAE	5.70	5.82	4.23	4.99	5.43	4.21	-	-	-	6.05	6.10	4.68	5.12	5.79	3.86

Table 5. Performance of point- and statistic- level metrics compared with contact solutions. (ME \pm STD and MAE in mmHg).

results directly extracted from the waveform estimations, including value, Bland-Altman, and correlation results. **(i) Statistic Value:** Discrete SBP and DBP values for Type I have low errors of (-1.80 ± 7.02) mmHg and (0.12 ± 5.40) mmHg, while those for Type II are (-1.54 ± 6.80) mmHg and (-0.50 ± 5.47) mmHg. Compared with contactless discrete BP estimation SOTA [60], WaveBP has a smaller MAE error but enables continuous waveform estimation. **(ii) Statistic Bland-Altman Plots:** Figure 16 (a)-(b) and Figure 17 (a)-(b) depict the Bland-Altman plots for SBP and DBP estimations directly extracted from the output waveforms of Type I and Type II. The x-axis represents the average of the estimated BP values and ground truth values, while the y-axis shows the estimation error. The top and bottom red dashed lines are the limits of agreement ($ME \pm 1.96 * STD$), indicating that over 95% of points fall within these limits, while the middle gray dashed line represents the mean error. **(iii) Statistic Correlation:** Figure 16 (c)-(d) and Figure 17 (c)-(d) display the statistic-level correlation PCC_s of SBP and DBP estimations compared to their references. Both schemes have high correlations with their references: SBP and DBP correlations are 0.86 and 0.85 for Type I and 0.86 and 0.84 for Type II, respectively.

7.3 Comparison with Contact Solutions

WaveBP achieves ABPW monitoring in a contactless manner which avoids the inconvenience of contact solutions [13, 16, 30, 35, 40]. It is important to understand its performance by comparison with existing contact solutions. We compare WaveBP with three contact solutions, including Crisp-BP [7], V-Net [17] trained on our dataset and our ECG/PPG-based teacher model. Crisp-BP [7] achieves advancing discrete BP estimation through a PPG sensor while V-Net [17] is a leading continuous ABPW monitoring model with ECG/PPG signals. The results are summarized in Table 5. For the discrete SBP/DBP estimation, both schemes of WaveBP achieve a smaller $ME \pm STD$ error than Crisp-BP [7] and V-Net [17], which could validate the effectiveness of our model design that improves the mmWave sensing capability. With the similar model design, WaveBP (Type I)'s MAE error is 0.58 mmHg higher than that of our ECG/PPG teacher model. This contactless performance can be improved to be comparable with the teacher with the benefits of Type II personalization.

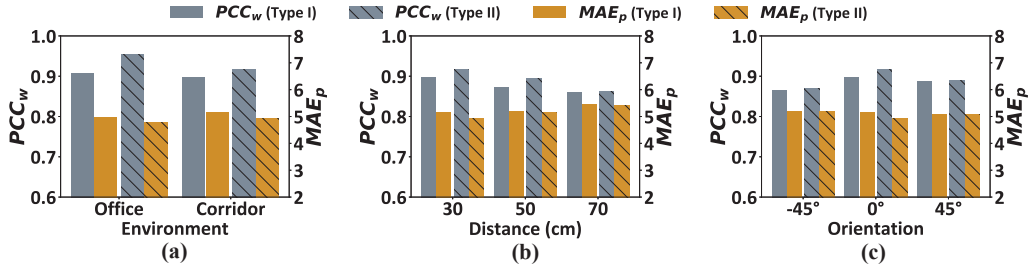


Fig. 18. (a) Impact of environment; (b) Impact of distance; (c) Impact of user orientation.

7.4 Robustness Study

To evaluate the robustness of WaveBP, we randomly selected 5 subjects from the 43 subjects with different health conditions. Each subject was chosen from the corresponding blood pressure (BP) categories: three with normal BP, one with elevated BP, and one in hypertension stage 1. Both schemes of WaveBP for the robustness study were trained only in the basic scenario of a common office and had never seen the test data. We use the waveform correlation PCC_w and the stricter metric MAE_p to compare the performance across different scenarios.

7.4.1 Impact of Environment. We evaluate the performance across two different environments, an office room and an indoor corridor with a fixed distance of 30 cm and orientation of 0°. The results in Figure 18(a) show that both schemes perform consistently well in both environments, with a minimal variation in MAE_p (within 0.5 mmHg). This indicates that our system focuses on signals from the subject's chest and the reflected signals are resilient to environmental influences.

7.4.2 Impact of Distance. Distance is a crucial factor of contactless sensing adoption in the real world. We evaluate our system at different distances by adjusting the distance between the radar and the subject from 30 cm to 70 cm in the corridor environment with a fixed orientation of 0°. As shown in Figure 18(b), both schemes have a high PCC_w of around 0.85 and their MAE_p errors increase no larger than 0.5 mmHg, which proves our system's robustness even under a long distance of 70 cm.

7.4.3 Impact of Orientation. As our system estimates ABPW from reflected signals of the chest, different subject orientations may affect its performance. To evaluate this, we fix the distance at 30 cm and ask subjects to vary their orientations from -45° to 45°, where the angle is defined as the angle between the radar-to-user line and the normal to the user's chest, and a positive angle indicates a clockwise rotation. The results, shown in Figure 18(c), suggest that both schemes maintained a high PCC_w of over 0.860 and MAE_p increased by no more than 0.5 mmHg across different orientation angles. This validates the effectiveness of imposing consistency constraints across different angles from BeamDA, particularly considering that both schemes were only trained with data at an orientation of 0° from 6 months ago.

7.4.4 Impact of Human Walking Around. As there may be other dynamic influences in the real world, it is important to be resilient to this influence. To validate this, we evaluate the performance with the disturbance of other subjects. We conduct this experiment with three subjects. In this case, the target subject sits at 30 cm of the radar with 0° orientation. We ask another subject to walk behind the target subject at a distance of 1 m. As shown in Figure 19(a), the performance of both Type I and Type II has a stable performance that the PCC_w is over 0.875 and the MAE_p increases by around 0.5 mmHg. This slight impact validates our system's robustness under dynamic multipaths caused by other moving subjects.

7.4.5 Impact of Varying User Statuses. As users' ABPWs may change with different conditions, it is important to validate the system's robustness under varying user statuses. We ask three subjects with normal BP, elevated BP,

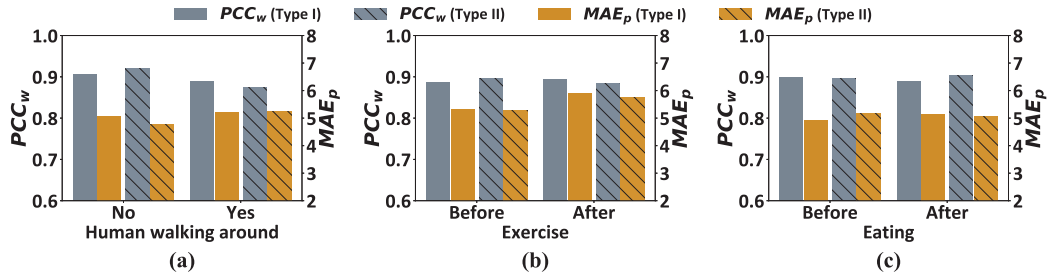


Fig. 19. (a) Impact of adjacent human walking around; (b) Impact of exercise; (c) Impact of eating.

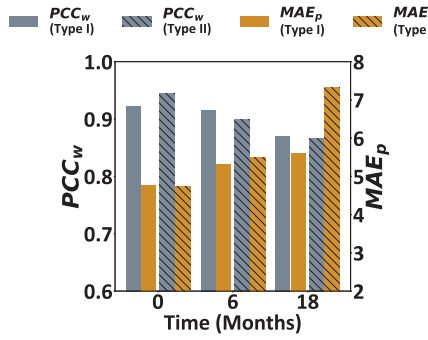


Fig. 20. Longitudinal Study.

BP-Category		Normal	Elevated	HS-1
ABPW Dist. (Mean \pm STD)	Month-0	92.1 ± 14.5	96.7 ± 13.8	101.1 ± 15.1
	Month-6	86.1 ± 10.8	99.9 ± 11.9	95.5 ± 14.7
ΔMAE_p	Type I	1.23	-0.36	0.35
	Type II	2.05	0.17	-0.66
ΔPCC_w	Type I	-0.027	0.018	0.003
	Type II	-0.034	-0.054	-0.045

Table 6. Temporal distribution impact on WaveBP. ‘Dist.’ is short for ‘Distribution’. ‘ Δ ’ indicates performance change.

and hypertension stage-1 respectively to change their states with two activities. One is exercise and the other is eating, as both can change the user’s blood pressure [1, 11]. The experiments were conducted when the users were still and at rest, as required by the standard measurement procedure [55]. The stable performance shown in Figure 19(b)-(c) could demonstrate WaveBP’s robustness under varying user conditions.

Impact of Exercise. To evaluate the effect of exercise, we collect the data when the subject is at rest before exercise and the data when the subject is at rest after a period of 5-min exercise during which the heart rate is over 140 beats per minute. The average ABPW of the states before exercise and after exercise is 95.44 and 98.33 mmHg, respectively. As shown in Figure 19(b), PCC_w of both schemes is stable with around 0.01 variation while the MAE_p errors slightly increase by around 0.7 mmHg. Compared with Type I, Type II has a smaller error increase with the benefits of personalization.

Impact of Eating. We collect data when the subject is fasting before the dinner and the data 15 minutes after the dinner. The average ABPW of the states before eating and after eating is 95.25 and 92.18 mmHg, respectively. Figure 19(c) demonstrates a stable performance of the two schemes that MAE_p changes within 0.3 mmHg and PCC_w maintains a high correlation above 0.890.

7.5 Longitudinal Study

It is important to prove the permanence of WaveBP’s generalizability on individuals’ ABPW shifts over time. To conduct the longitudinal study, we randomly select 3 subjects including one with normal BP, one with elevated BP, and one in hypertension stage 1 (HS-1) to evaluate the trained model over long periods. We collect the data from the subjects after 6 and 18 months and directly test the previously trained model. As shown in Figure 20, the MAE_p error of Type I increases 0.56 mmHg and 0.85 mmHg for 6 months and 18 months after the first data collection while the PCC_w of Type I decreases 0.007 and 0.053, respectively. The MAE_p error of Type II increases by 0.75 mmHg and 2.59 mmHg after 6 months and 18 months while the PCC_w of Type I decreases by 0.045 and

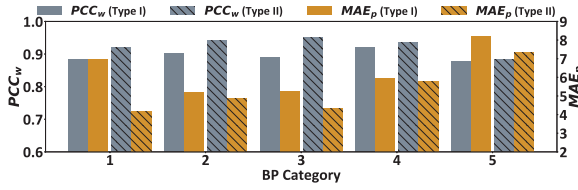


Fig. 21. Performance of different BP categories.

WaveBP	Cost
Inference Latency	14.80 ms
GPU Memory	2192 MB

Table 7. Computational cost for deployment.

0.079, respectively. We could observe that Type I's performance is more stable than Type II's since it gets the user's latest BP category while Type II is ignorant of the user's state. Though TypeII's MAE_p increases to over 7mm Hg after 18 months of personalization, both schemes have stable performances over 6 months.

To deliver more insights on WaveBP's generalizability, we analyze the longitudinal study in detail about the subjects' ABPW distributions and corresponding impacts on WaveBP. The results in Table 6 show that the impacts of different BP categories are similar. The average ABPW distribution shifts of the normal person and the Hypertension Stage-1 subject after 6 months are around 6 mmHg while the maximum increased error is around 2 mmHg. Compared with the ABPW distribution shifts, the error changes of WaveBP are much more stable, which proves that WaveBP can reliably track ABPW rather than simply overfitting.

7.6 Performance Analysis on BP Categories

We compare the performances across the five BP categories: hypotension, normal, elevated, hypertension stage-1, and hypertension stage-2 blood pressure records corresponding to Category 1-5 in Figure 21. We observe that WaveBP can produce waveforms with high correlations over 0.870 and small MAE_p lower than 6.0 mmHg for Category 1-4 by combining the two schemes. Compared with our Type I scheme, our Type II has lower errors for Category 1 since it is retrained with more target users' data. However, both schemes have larger MAE_p errors in Category 5. Despite the error of hypertension-stage-2, the overall probability of error(≤ 10 mmHg) is 86.65% and acceptable by the standard BP protocol [55]. One possible reason is the highly imbalanced distribution that the Category 5's readings are much fewer than those in other categories as illustrated in Figure 13.

7.7 Computational Cost

Though trained on a powerful GPU RTX 3090 server, WaveBP is expected to perform inference with low computational cost. To prove the practical usage of WaveBP , we conduct inference measurement by averaging 1000 sequential samples' results with the RTX 3090 GPU card. As shown in Table 7, the inference latency is 14.80 ms for one 8-second input, which proves that WaveBP can work in real time. Furthermore, the low GPU memory requirement of 2192 MB is affordable for most consumer-grade GPU cards. The reason why WaveBP can achieve both sides of good performance and a low computational cost is that mmFormer is mostly enhanced by BeamDA and CMKT in the training stage without introducing extra burden for practical deployment.

7.8 Ablation Study

We conduct ablation studies to understand the contributions of different components of WaveBPwith metrics including mean absolute error (MAE_p), the standard deviation of mean absolute error of each point in the waveform (STD_w), and the waveform correlation (PCC_w). We also evaluate whether the extracted statistic-level SBP and DBP estimations satisfy AAMI's requirement.

Table 8 shows that our system achieves the best performance within AAMI's boundary when all modules are used (Case 5 for Type I and Case 6 for Type II schemes) for mmWave signals. The shortcut architecture and personalization mechanism significantly improve performance compared to Case 1-3, validating our multi-resolution design and the necessity of personalization. Compared to Cases 3 and 4, CMKT can greatly reduce the

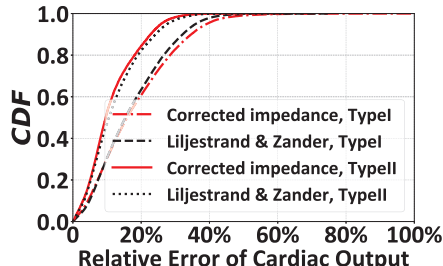
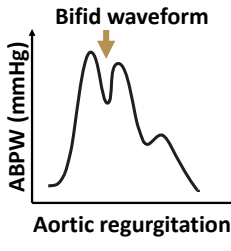


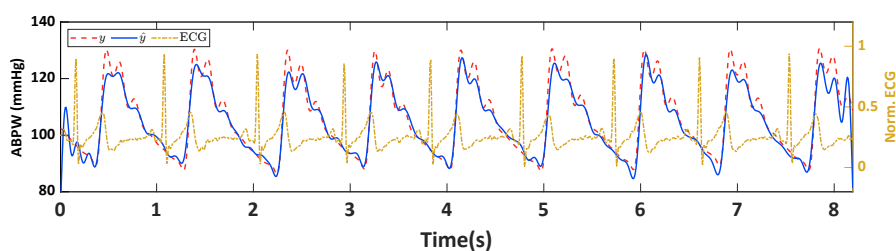
Fig. 22. Case study 1: relative cardiac output means a better performance. PT is short for Personalization Type. "AAMI" means whether satisfy AAMI's requirement.

Case	Shortcuts	BeamDA	CMKT	PT	$MAE_{p\downarrow}$	$STD_{w\downarrow}$	$PCC_{w\uparrow}$	AAMI
1	✗	✗	✗	✗	12.25	9.68	0.523	✗
2	✓	✗	✗	✗	10.48	8.32	0.861	✗
3	✓	✗	✗	I	7.77	6.35	0.870	✗
4	✓	✗	✓	I	7.17	5.90	0.881	✗
5	✓	✓	✓	I	5.70	4.84	0.903	✓
6	✓	✓	✓	II	4.99	4.27	0.935	✓
Teacher	✓	✗	✗	I	5.12	4.06	0.936	✓

Table 8. Results of ablation studies. "↓" indicates a lower error, while "↑" means whether satisfy AAMI's requirement.



(a) AR illustration [9].



(b) ABPW of a subject with aortic regurgitation (AR).

Fig. 23. Case study 2: ABPW could reflect cardiac abnormality. (a): An illustration of AR from medical reference [9]. (b): Estimation of WaveBP for a subject in hypertension stage-1 with AR. y is the ABPW ground truth and \hat{y} is WaveBP's estimation (Type II). ECG is the corresponding electrocardiogram signal, which may not be non-specific to AR [38].

error and enhance the estimation stability, indicating that CMKT as regularization is effective and can supplement extra information for better pressure value preservation. BeamDA can further improve reliability by reducing the absolute value error and its standard deviation (Cases 4 and 5). Furthermore, the performance can be improved to be comparable with the contact ECG/PPG-based teacher model with Type I personalization (Case 6 and the teacher model) when the general model in Case 5 is tailored for the user.

7.9 Case Studies

WaveBP extends the contactless cardiac sensing with ABPW monitoring. To validate its significance and applicability, we conduct three case studies. Case Studies 1 and 2 show the significance of ABPW by its potential for fine-grained cardiac indicator estimation and cardiac abnormality detection. Case 3 presents the applicability of a usage scenario that monitors a subject's ABPW while watching TV without any disturbances.

7.9.1 Case Study 1: Relative Cardiac Output through ABPW. To illustrate the importance of ABPW, we conduct a case study to calculate the relative cardiac output using the estimated ABPW from the two schemes and the reference ABPW. The relative cardiac output error [56] is defined as $r = \frac{|G(\hat{y}) - G(y)|}{G(y)}$, where G is the algorithm to estimate cardiac output (CO) from ABPW, \hat{y} and y are the estimated ABPW and the reference ABPW, respectively.

We calculate the relative error r from the estimated results of the 43 subjects based on the two best CO estimators from the previous work [56], including Liljestrand & Zadnder formula [31] and corrected impedance formula [62], as shown in Figure 22. The mean errors of the relative cardiac output results for Type I and Type II are 17.1% and 18.0% with the Liljestrand & Zadnder formula and 11.4% and 12.3% with the corrected impedance formula, respectively. This low error indicates that the CO from our estimated ABPW has a good agreement with that from the reference ABPW [44]. Despite the intrinsic error from the CO estimator, it shows a promising

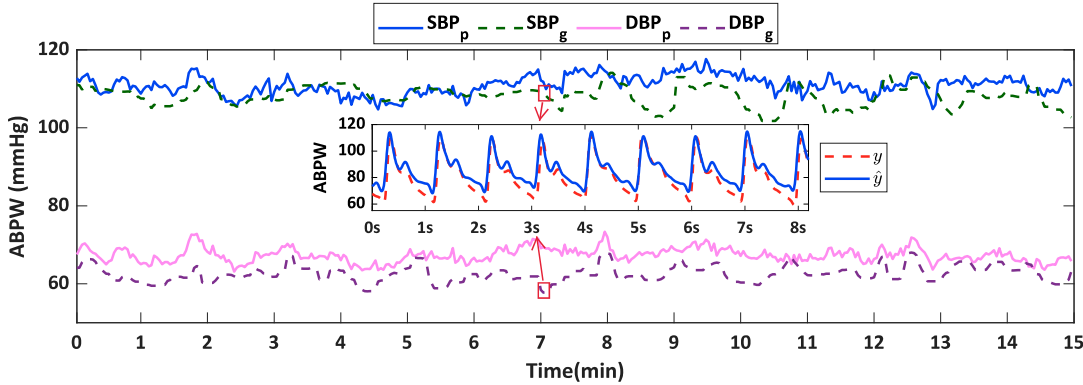


Fig. 24. Case Study 3: Long-time ABPW Monitoring. SBP_p , DBP_p , and SBP_g , DBP_g are WaveBP’s discrete SBP/DBP extracted from the ABPW estimations and the corresponding ground truth, respectively. \hat{y} and y are the WaveBP’s ABPW estimation and ground truth at the 7th minute, respectively.

direction that we could further leverage the sensed ABPW from WaveBP to monitor fine-grained hemodynamic indicators for preventing heart diseases in a contactless manner.

7.9.2 Case Study 2: Cardiac Abnormality Detection through ABPW. Compared with discrete BP values, ABPW reflects cardiac abnormalities. To validate its effectiveness, we collect data from a subject with chronic aortic regurgitation (AR), which is a type of heart valve disease. AR indicates that the valve between the lower left heart chamber and the main artery of the body does not close tightly, causing the blood pumped out of the left ventricle to leak backward [38]. This disease may lead to pulmonary edema and even cardiogenic shock. Compared with ECG which may be non-specific to AR, ABPW is a good indicator of AR with widened pulse pressure [38]. During the cardiac cycle, the blood will first be pumped out of the left ventricle with a high peak in ABPW. Then the blood that leaks backward due to AR causes the second peak, resulting in the bifid waveform pattern as shown in Figure 23(a). The discrete SBP/DBP of this subject is 131/86 mmHg, only indicating the hypertension stage-1, while his ABPW indicates finer-grained cardiac dynamics with abnormal blood leaking backward as shown in Figure 23(a). Compared with ground truth, the ABPW estimate of WaveBP (Type II) in Figure 23(b) can well capture the bifid waveform feature with a high PCC_w of 0.971 and a low MAE_p of 2.28 mmHg, confirming the potential for the detection of cardiac abnormalities through contactless ABPW monitoring.

7.9.3 Case Study 3: Long-time Monitoring for a User Watching TV. To validate the real-world applicability, we ask one volunteer to watch TV in front of the radar which is placed 50 cm in front of him. We use 18 minutes of data for Type II personalization and then deploy the radar to contactlessly track his ABPW. The only requirement is to avoid large motions which is for both our system and the reference equipment. As shown in Figure 24, WaveBP’s ABPW estimations are consistent with the ground truth, which indicates that WaveBP can accurately track a user’s BP variation. Specifically, The MAE of SBP and DBP predictions are 3.44 mmHg and 4.81 mmHg, respectively. Besides a low error of discrete SBP and DBP estimations, WaveBP can achieve a low MAE error of point-level predictions as 4.80 mmHg and a high waveform correlation of 0.958. This case study mimics a typical usage scenario for WaveBP and validates its applicability for long-time non-intrusive monitoring.

8 DISCUSSION AND FUTURE WORK

8.1 Usage Scenario

Our system assumes that the user sits before the radar to sense the chest movement. Existing contact solutions based on expensive volume-clamp (~40K USD) or wearables [41] exert high pressure or require close contact,

thus introducing uncomfortable experiences and may not suit subjects with sensitive skins. As the first step of contactless ABPW sensing, WaveBP only requires 8 seconds of relatively still sitting, making it suitable for broader scenarios like sleeping. Though the robustness study demonstrates that our system is resilient to orientation variations to 90 degrees and distance variations from 30 cm to 70 cm, which is suitable for typical ABPW monitoring, it is also important to extend our system to more diverse daily scenarios, such as different poses and multiple users, which will be conducted in our future work.

8.2 Ease of Calibration

To mitigate the blood pressure distribution shifts caused by physiological divergence, we design two schemes with the balance of data collection burdens. Our Type I scheme has the same calibration frequency requirement as our reference device, CNAP Monitor 100D [20] which requires calibration for every test while our Type II only requires one-time calibration for six months with around 20 minutes ABPW data for personalization. To make WaveBP more deployable, it is always desired to reduce users' efforts for convenient experiences. We think this problem falls in the scope of model generalization with few samples. In our future work, we plan to eliminate the personalization efforts by few-shot learning combined with transfer learning techniques [12, 57] to help the model generalize to new subjects with limited samples.

8.3 More Diverse User Distribution

Currently, our prototype is evaluated on 43 subjects with a blood pressure range from 41 mmHg to 156 mmHg, including some hypotension and hypertension ABPW readings. The evaluations validate the reliability of our system for subjects with a wide range of daily life. However, as shown in Section 7.6, our performance is not ideal for hypertension stage-2 readings because of highly imbalanced data distribution shown in Figure 13, which is an open issue for machine learning techniques [32]. One promising direction to enhance WaveBP is to acquire more diverse data distributions. We envision this could be mitigated through data collection on a larger number of diverse subjects, data generation [64] and re-balancing strategies [68], and leave it for future improvement.

8.4 User Experience Study

WaveBP aims to release contact burdens through mmWave signals. Extensive experiments have validated its benefits and practicality in daily life. We would like to discuss user experience from the experiments. Firstly, WaveBP shares the common requirement with current medical BP systems that the user should avoid large motions during the 8 seconds of measurement. We observe that users can easily keep still with the monitoring instructions informed. In the future, WaveBP can incorporate the widely applied activity recognition system to detect whether this requirement is satisfied for better user interactions. Secondly, there still exists space to improve user experience. The system currently analyzes the ABPW in the offline mode, even though we show through simulation that WaveBP supports real-time operations. Future work could consider making the system work in real-time so that it can provide more intuitive and quick feedbacks. Besides, the form factor of the radar can be optimized. Despite the flexible development benefit of the radar used in this work (TI IWR1443 [23] and DCA1000EVM [22]), some users think the radar is rarely seen in the households and may distract their attention in daily life activities such as watching TV. We envision that future work can consider the use of a smaller radar or investigate the feasibility of embedding the radar device in a more natural way.

9 RELATED WORKS

9.1 ABPW and Discrete BP Measurement

In this section, we will review the current technologies with their advantages and shortcomings for discrete blood pressure and ABPW measurement in different scenarios.

Invasive arterial line. As the gold standard method for ABPW measurement, it uses a pressure transducer with a catheter inserted into the artery and measures the pressure directly [45]. Though accurate, it is mainly limited to ICU scenarios for its invasiveness.

Cuff-based measurement. The auscultatory and oscillometric devices [5] are the two most common non-invasive blood pressure measurement methods. Both methods use an inflatable cuff wrapped around the user's upper arm to occlude the artery. Though less invasive than the arterial line, they cannot provide continuous blood pressure waveform due to the long-time scanning. The volume clamp technology [41] is proposed to provide non-invasive ABPW measurement. It involves a cuff inflating the fingers and a PPG sensor detecting arterial expansion and then measures continuous blood pressure variations with a standard inflatable cuff device for calibration. However, these devices are usually bulky and expensive, making them inconvenient for daily usage.

Wearable measurement. Physiological signals (*e.g.*, ECG and PPG) can be analyzed for more convenient blood pressure measurement. Pulse transit time, the time delay that a pressure wave travels between two separate arterial sites, is one of the most promising features related to blood pressure [3, 42]. PTT can be calculated from PPG and/or ECG sensors to reveal the speed of the pressure propagating along the arterial wall. Physiological modeling and deep learning methods are explored to build the relationship between PPG, ECG, blood pressure, and ABPW [7, 12, 17]. To mitigate the calibration issues of ECG/PPG methods, FewshotBP [12] introduces a personalization adapter that enables model personalization with a small amount of target user's data. Similar to the PPG method, Johnson et al. [26] uses a mmWave sensor contact to the wrist to estimate ABPW. Wang et al. [59] uses the IMU sensor inside the phone to estimate discrete BP and requires to press the phone against the chest. However, the wearable methods experience degraded performance under imperfect contact with the sensors [13, 35, 39]. Continuous close skin contact is also uncomfortable for daily usage and may even cause skin irritation [13, 16, 30, 35, 40].

Contactless measurement. Contactless blood pressure measurement methods have recently gained attention due to their significant convenience. Remote photoplethysmography (rPPG) has been developed to extract information from videos with a camera. Fluctuations in light intensity or frequency domains have been studied to estimate blood pressure from rPPG [64]. However, rPPG-based methods are sensitive to ambient light conditions and may raise privacy concerns. Alternatively, radio frequency-based methods have been developed to estimate discrete blood pressure values [8, 24, 28, 35, 52, 54]. Nevertheless, these methods are mainly based on the PTT-like principle and thus need a long period (one heartbeat to 30 seconds) to derive one discrete BP value, which cannot achieve the sequence mapping requirement of ABPW monitoring as shown in Table 1. Besides, previous works require good-quality mmWave signals which restrict the user to fix their hand around a specific position [8, 35, 52] or require dedicated hardware [24]. Recently, RF-BP [60] releases the fixed hand requirement by placing a UWB radar towards a sitting subject. However, it still requires 30 seconds to select an 8-second clean sample and then combine multiple cardiac cycles inside the sample to estimate one discrete SBP/DBP value, which cannot fulfill the high sampling rate of ABPW. Different from them, our system extends the contactless monitoring capability from discrete BP values to continuous ABPWs, which holds great potential of fine-grained cardiac indicator estimation and cardiac abnormality detection beyond the discrete BP estimation.

9.2 mmWave Cardiac Sensing

Contactless cardiac sensing has attracted much attention and the mmWave signal is regarded as one of the most promising modalities with its high precision. Recently, the mmWave signal has been exploited to detect biomarkers and monitor key vital signs. Based on the cardiac-mmWave scattering effect, CardiacWave [65] infers detailed ECG-like heart activities with an LSTM-based neural network. VitaNet [29] transforms chest vibrations into PPG-like signals with an encoder-decoder framework. mmArrhythmia [72] performs multi-channel ensemble learning to detect arrhythmia. RF-SCG [16] adopts a CNN-based model to translate chest vibrations into SCG

signals to detect mechanical cardiac events. Zhang et al. [71] leverage the advanced variational encoder-decoder to recover PPG-like waveform from mmWave signals. WaveBP differs from previous works in two aspects. Firstly, from the scenario aspect, WaveBP extends the scope of contactless cardiac sensing as arterial blood pressure waveform can describe detailed cardio-dynamics as it can directly indicate abnormal blood pressure like hypertension and abnormal cardiovascular conditions [9] as illustrated in Section 2.2. Secondly, since ABPW requires accurate estimation for both pressure values and waveform shapes while ECG/PPG/SCG-like signals only require accurate shapes, it is more challenging for contactless ABPW monitoring. From the technique aspect, different from previous works that are mainly based on neural networks with one-level bottleneck with a coarse resolution, WaveBP designs a hybrid transformer featured with multiple resolution aggregation that could benefit more comprehensive temporal analysis. Besides, WaveBP reduces the requirement of high-quality data with the theoretically guaranteed BeamDA and compensates for extra information from other modalities with CMKT. Our ablation study in Section 7.8 highlights the effectiveness of the three essential designs.

10 CONCLUDING REMARKS

This work presents the first contactless arterial blood pressure waveform monitoring with a commercial mmWave radar. We start from analyzing the correlations between mmWave and ABPW with a hemodynamics model. To convert one heartbeat's mmWave sequences to ABPW sequences, we propose a hybrid deep learning pipeline including the backbone model mmFormer with multi-resolution awareness and practical personalization schemes, the data augmentation method BeamDA for robustness enhancement, and CMKT for knowledge fusion without extra efforts for deployment. The evaluation results prove that our system achieves accurate and robust ABPW estimation and holds great potential for cardiovascular status monitoring, cardiac abnormality detection and long-time monitoring, as evidenced by our case studies.

ACKNOWLEDGMENTS

The authors would like to thank Wenqian Li from School of Medicine, Zhejiang University and Shirong Qiu from CUHK for their helpful comments from medical and bioengineering perspectives. We also thank the Turing AI Computing Cloud (TACC) [67] and HKUST iSING Lab for providing computation resources on their platform. This research is supported in part by RGC under Contract CERG 16206122, 16204523, AoE/E-601/22-R, R6021-20, and Contract R8015.

REFERENCES

- [1] Lawrence J Appel, Thomas J Moore, Eva Obarzanek, William M Vollmer, Laura P Svetkey, Frank M Sacks, George A Bray, Thomas M Vogt, Jeffrey A Cutler, Marlene M Windhauser, et al. 1997. A clinical trial of the effects of dietary patterns on blood pressure. *New England journal of medicine* 336, 16 (1997), 1117–1124.
- [2] Tasbiraha Athaya and Sunwoong Choi. 2022. A Review of Noninvasive Methodologies to Estimate the Blood Pressure Waveform. *Sensors* 22, 10 (2022), 3953.
- [3] Daniel Barvik, Martin Cerny, Marek Penhaker, and Norbert Noury. 2021. Noninvasive continuous blood pressure estimation from pulse transit time: A review of the calibration models. *IEEE Reviews in Biomedical Engineering* 15 (2021), 138–151.
- [4] SN Bhuiya, F Islam, and MA Matin. 2012. Analysis of direction of arrival techniques using uniform linear array. *International Journal of Computer Theory and Engineering* 4, 6 (2012), 931–934.
- [5] P Bonnafoix. 1996. Auscultatory and oscillometric methods of ambulatory blood pressure monitoring, advantages and limits: a technical point of view. *Blood pressure monitoring* 1, 3 (1996), 181–185.
- [6] Nam Bui, Nhat Pham, Jessica Jacqueline Barnitz, Zhanan Zou, Phuc Nguyen, Hoang Truong, Taeho Kim, Nicholas Farrow, Anh Nguyen, Jianliang Xiao, Robin R. Deterding, Thang N. Dinh, and Tam Vu. 2019. eBP: A Wearable System For Frequent and Comfortable Blood Pressure Monitoring From User's Ear. In *MobiCom*. ACM, 53:1–53:17.
- [7] Yetong Cao, Huijie Chen, Fan Li, and Yu Wang. 2021. Crisp-BP: continuous wrist PPG-based blood pressure measurement. In *MobiCom*. ACM, 378–391.

- [8] Yetong Cao, Shujie Zhang, Fan Li, Zhe Chen, and Jun Luo. 2024. hBP-Fi: Contactless Blood Pressure Monitoring via Deep-Analyzed Hemodynamics. In *INFOCOM*. IEEE, 1211–1220.
- [9] David Chambers, Christopher Huang, and Gareth Matthews. 2019. *Basic physiology for anaesthetists*. Cambridge University Press.
- [10] Thiago Bulhões da Silva Costa, Felipe Meneguitti Dias, Diego Armando Cardona Cárdenas, Marcelo Toledo, Daniel Mario de Lima, José Eduardo Krieger, and Marco Antonio Gutierrez. 2023. Blood Pressure Estimation From Photoplethysmography by Considering Intra- and Inter-Subject Variabilities: Guidelines for a Fair Assessment. *IEEE Access* 11 (2023), 57934–57950.
- [11] Keith M Diaz and Daichi Shimbo. 2013. Physical activity and the prevention of hypertension. *Current hypertension reports* 15 (2013), 659–668.
- [12] Feiyi Fan, Yang Gu, Jianfei Shen, Fan Dong, and Yiqiang Chen. 2023. FewShotBP: Towards Personalized Ubiquitous Continuous Blood Pressure Measurement. *Proc. ACM Interact. Mob. Wearable Ubiquitous Technol.* 7, 3 (2023), 94:1–94:39.
- [13] Jesse Fine, Kimberly L Branan, Andres J Rodriguez, Tananant Boonya-Ananta, Ajmal, Jessica C Ramella-Roman, Michael J McShane, and Gerard L Cote. 2021. Sources of inaccuracy in photoplethysmography for continuous cardiovascular monitoring. *Biosensors* 11, 4 (2021), 126.
- [14] Eoin Finnegan, Shaun Davidson, Mirae Harford, Peter Watkinson, Lionel Tarassenko, and Mauricio Villarroel. 2023. Features from the photoplethysmogram and the electrocardiogram for estimating changes in blood pressure. *Scientific Reports* 13, 1 (2023), 986.
- [15] John M Flack and Bemi Adekola. 2020. Blood pressure and the new ACC/AHA hypertension guidelines. *Trends in cardiovascular medicine* 30, 3 (2020), 160–164.
- [16] Unsoo Ha, Salah Assana, and Fadel Adib. 2020. Contactless seismocardiography via deep learning radars. In *MobiCom*. ACM, 62:1–62:14.
- [17] Brian L Hill, Nadav Rakocz, Ákos Rudas, Jeffrey N Chiang, Sidong Wang, Ira Hofer, Maxime Cannesson, and Eran Halperin. 2021. Imputation of the continuous arterial line blood pressure waveform from non-invasive measurements using deep learning. *Scientific reports* 11, 1 (2021), 15755.
- [18] ANALOG DEVICES Inc. 2022.03.31. AD8232. <https://www.analog.com/en/products/ad8232.html>.
- [19] BIOPAC Systems Inc. 2022.03.31. BIOPAC MP160 System. <https://www.biopac.com/product-category/research/systems/mp150-starter-systems/>.
- [20] BIOPAC Systems Inc. 2022.03.31. CNAP 100D Monitor. <https://www.biopac.com/product/noninvasive-blood-pressure-nibp100d/>.
- [21] Texas Instruments Inc. 2022.03.31. TI ADS1299EEGFE. <https://www.ti.com/cn/tool/cn/ADS1299EEGFE-PDK>.
- [22] Texas Instruments Inc. 2022.03.31. TI DCA1000EVM. <https://www.ti.com/tool/DCA1000EVM>.
- [23] Texas Instruments Inc. 2022.03.31. TI IWR1443BOOST. <https://www.ti.com/tool/IWR1443BOOST>.
- [24] Shuzo Ishizaka, Kohei Yamamoto, and Tomoaki Ohtsuki. 2021. Non-contact Blood Pressure Measurement using Doppler Radar based on Waveform Analysis by LSTM. In *ICC*. IEEE, 1–6.
- [25] Chengkun Jiang, Junchen Guo, Yuan He, Meng Jin, Shuai Li, and Yunhao Liu. 2020. mmVib: micrometer-level vibration measurement with mmwave radar. In *MobiCom*. ACM, 45:1–45:13.
- [26] Jessi E. Johnson, Oliver Shay, Chris Kim, and Catherine Liao. 2019. Wearable Millimeter-Wave Device for Contactless Measurement of Arterial Pulses. *IEEE Trans. Biomed. Circuits Syst.* 13, 6 (2019), 1525–1534.
- [27] Mohamad Kachuee, Mohammad Mahdi Kiani, Hoda Mohammadzade, and Mahdi Shabany. 2015. Cuff-less high-accuracy calibration-free blood pressure estimation using pulse transit time. In *ISCAS*. IEEE, 1006–1009.
- [28] Ryota Kawasaki and Akihiro Kajiwara. 2022. Continuous blood pressure estimation using millimeter wave radar. In *RWS*. IEEE, 135–137.
- [29] Usman Mahmood Khan, Luca Rigazio, and Muhammad Shahzad. 2022. Contactless Monitoring of PPG Using Radar. *Proc. ACM Interact. Mob. Wearable Ubiquitous Technol.* 6, 3 (2022), 123:1–123:30.
- [30] Kwang Bok Kim and Hyun Jae Baek. 2023. Photoplethysmography in wearable devices: a comprehensive review of technological advances, current challenges, and future directions. *Electronics* 12, 13 (2023), 2923.
- [31] Julian Koenig, LaBarron K Hill, DeWayne P Williams, and Julian F Thayer. 2015. Estimating cardiac output from blood pressure and heart rate: the Liljestrand & Zander formula. *Biomedical sciences instrumentation* 51 (2015), 85.
- [32] Bartosz Krawczyk. 2016. Learning from imbalanced data: open challenges and future directions. *Prog. Artif. Intell.* 5, 4 (2016), 221–232.
- [33] Bouchra Lamia, Denis Chemla, Christian Richard, and Jean-Louis Teboul. 2005. Clinical review: interpretation of arterial pressure wave in shock states. *Critical Care* 9, 6 (2005), 1–6.
- [34] Joon Lee, Daniel J Scott, Mauricio Villarroel, Gari D Clifford, Mohammed Saeed, and Roger G Mark. 2011. Open-access MIMIC-II database for intensive care research. In *2011 Annual International Conference of the IEEE Engineering in Medicine and Biology Society*. IEEE, 8315–8318.
- [35] Yumeng Liang, Anfu Zhou, Xinzhe Wen, Wei Huang, Pu Shi, Lingyu Pu, Huanhuan Zhang, and Huadong Ma. [n. d.]. airBP: Monitor Your Blood Pressure with Millimeter-Wave in the Air. *ACM Transactions on Internet of Things* ([n. d.]).
- [36] Yinji Ma, Jungil Choi, Aurélie Hourlier-Fargette, Yeguang Xue, Ha Uk Chung, Jong Yoon Lee, Xiufeng Wang, Zhaoqian Xie, Daeshik Kang, Heling Wang, et al. 2018. Relation between blood pressure and pulse wave velocity for human arteries. *Proceedings of the National Academy of Sciences* 115, 44 (2018), 11144–11149.

- [37] Sakib Mahmud, Nabil Ibtehaz, Amith Khandakar, M Sohel Rahman, Antonio JR Gonzales, Tawsifur Rahman, Md Shafayet Hossain, Md Sakib Abrar Hossain, Md Ahsan Atick Faisal, Farhan Fuad Abir, et al. 2023. NABNet: a nested attention-guided BiConvLSTM network for a robust prediction of blood pressure components from reconstructed arterial blood pressure waveforms using PPG and ECG signals. *Biomedical Signal Processing and Control* 79 (2023), 104247.
- [38] Gerald Maurer. 2006. Aortic regurgitation. *Heart* 92, 7 (2006), 994–1000.
- [39] Jesse McLaren. 2024.07.05. ECG Cases 29 Misdiagnosis from Lead Misplacement, Artifact and Lead Reversal. <https://emergencymedicinecases.com/ecg-cases-lead-misplacement-artifact-lead-reversal/>.
- [40] Stanford Medicine. 2024.07.05. Risks of Electrocardiograms. <https://stanfordhealthcare.org/medical-tests/e/ekg/risks.html>.
- [41] Agnes S Meidert and Bernd Saugel. 2018. Techniques for non-invasive monitoring of arterial blood pressure. *Frontiers in medicine* 4 (2018), 231.
- [42] Ramakrishna Mukkamala, Jin-Oh Hahn, Omer T. Inan, Lalit K. Mestha, Chang-Sei Kim, Hakan Toreyin, and Survi Kyal. 2015. Toward Ubiquitous Blood Pressure Monitoring via Pulse Transit Time: Theory and Practice. *IEEE Trans. Biomed. Eng.* 62, 8 (2015), 1879–1901.
- [43] Mahesh Nirmalan and Paul M Dark. 2014. Broader applications of arterial pressure wave form analysis. *Continuing Education in Anaesthesia, Critical Care & Pain* 14, 6 (2014), 285–290.
- [44] Peter M Odor, Sohail Bampoe, and Maurizio Cecconi. 2017. Cardiac output monitoring: Validation studies—how results should be presented. *Current anesthesiology reports* 7 (2017), 410–415.
- [45] John C O'Horo, Dennis G Maki, Anna E Krupp, and Nasia Safdar. 2014. Arterial catheters as a source of bloodstream infection: a systematic review and meta-analysis. *Critical care medicine* 42, 6 (2014), 1334–1339.
- [46] Mark A Richards. 2014. *Fundamentals of radar signal processing*. McGraw-Hill Education.
- [47] Adriana Romero, Nicolas Ballas, Samira Ebrahimi Kahou, Antoine Chassang, Carlo Gatta, and Yoshua Bengio. 2015. FitNets: Hints for Thin Deep Nets. In *ICLR (Poster)*.
- [48] Olaf Ronneberger, Philipp Fischer, and Thomas Brox. 2015. U-Net: Convolutional Networks for Biomedical Image Segmentation. In *MICCAI (3) (Lecture Notes in Computer Science, Vol. 9351)*. Springer, 234–241.
- [49] Gianluigi Savarese, Peter Moritz Becher, Lars H Lund, Petar Seferovic, Giuseppe MC Rosano, and Andrew JS Coats. 2022. Global burden of heart failure: a comprehensive and updated review of epidemiology. *Cardiovascular research* 118, 17 (2022), 3272–3287.
- [50] Fabian Schrumpf, Patrick Frenzel, Christoph Aust, Georg Osterhoff, and Mirco Fuchs. 2021. Assessment of deep learning based blood pressure prediction from PPG and rPPG signals. In *Proceedings of the IEEE/CVF Conference on Computer Vision and Pattern Recognition*. 3820–3830.
- [51] Fabian Schrumpf, Paul Rudi Serdack, and Mirco Fuchs. 2022. Regression or Classification? Reflection on BP prediction from PPG data using Deep Neural Networks in the scope of practical applications. In *Proceedings of the IEEE/CVF Conference on Computer Vision and Pattern Recognition*. 2172–2181.
- [52] Zhenguo Shi, Tao Gu, Yu Zhang, and Xi Zhang. 2022. mmBP: Contact-Free Millimetre-Wave Radar Based Approach to Blood Pressure Measurement. In *SensSys*. ACM, 667–681.
- [53] Boris Shirokikh, Ivan Zakazov, Alexey Chernyavskiy, Irina Fedulova, and Mikhail Belyaev. 2020. First U-Net Layers Contain More Domain Specific Information Than the Last Ones. In *DART/DCL@MICCAI (Lecture Notes in Computer Science, Vol. 12444)*. Springer, 117–126.
- [54] Lovedeep Singh, Sungjin You, Byung Jang Jeong, Chiwan Koo, and Youngwook Kim. 2023. Remote Estimation of Blood Pressure Using Millimeter-Wave Frequency-Modulated Continuous-Wave Radar. *Sensors* 23, 14 (2023), 6517.
- [55] George S Stergiou, Bruce Alpert, Stephan Mieke, Roland Asmar, Neil Atkins, Siegfried Eckert, Gerhard Frick, Bruce Friedman, Thomas Graßl, Tsutomu Ichikawa, et al. 2018. A universal standard for the validation of blood pressure measuring devices: Association for the Advancement of Medical Instrumentation/European Society of Hypertension/International Organization for Standardization (AAMI/ESH/ISO) Collaboration Statement. *Hypertension* 71, 3 (2018), 368–374.
- [56] JX Sun, AT Reisner, M Saeed, and RG Mark. 2005. Estimating cardiac output from arterial blood pressurewaveforms: a critical evaluation using the MIMIC II database. In *Computers in Cardiology, 2005*. IEEE, 295–298.
- [57] Qianru Sun, Yaoyao Liu, Tat-Seng Chua, and Bernt Schiele. 2019. Meta-Transfer Learning for Few-Shot Learning. In *CVPR. Computer Vision Foundation / IEEE*, 403–412.
- [58] Ashish Vaswani, Noam Shazeer, Niki Parmar, Jakob Uszkoreit, Llion Jones, Aidan N. Gomez, Łukasz Kaiser, and Illia Polosukhin. 2017. Attention is All you Need. In *NIPS*. 5998–6008.
- [59] Lei Wang, Xingwei Wang, Yu Zhang, Xiaolei Ma, Haipeng Dai, Yong Zhang, Zhijun Li, and Tao Gu. 2024. Accurate Blood Pressure Measurement Using Smartphone's Built-in Accelerometer. *Proc. ACM Interact. Mob. Wearable Ubiquitous Technol.* 8, 2 (2024), 57:1–57:28.
- [60] Zhi Wang, Beihong Jin, Fusang Zhang, Siheng Li, and Junqi Ma. 2024. UWB-enabled Sensing for Fast and Effortless Blood Pressure Monitoring. *Proc. ACM Interact. Mob. Wearable Ubiquitous Technol.* 8, 2 (2024), 65:1–65:26.
- [61] Thomas Weber and Julio A Chirinos. 2018. Pulsatile arterial haemodynamics in heart failure. *European heart journal* 39, 43 (2018), 3847–3854.
- [62] KH Wesseling. 1983. A simple device for the continuous measurement of cardiac output. *Adv Cardiovasc Phys* 5 (1983), 16–52.

- [63] Nico Westerhof, Jan-Willem Lankhaar, and Berend E Westerhof. 2009. The arterial windkessel. *Medical & biological engineering & computing* 47, 2 (2009), 131–141.
- [64] Bing-Fei Wu, Li-Wen Chiu, Yi-Chiao Wu, Chun-Chih Lai, and Pao-Hsien Chu. 2022. Contactless Blood Pressure Measurement via Remote Photoplethysmography with Synthetic Data Generation Using Generative Adversarial Network. In *CVPR Workshops*. IEEE, 2129–2137.
- [65] Chenhan Xu, Huining Li, Zhengxiong Li, Hanbin Zhang, Aditya Singh Rathore, Xingyu Chen, Kun Wang, Ming-Chun Huang, and Wenyao Xu. 2021. CardiacWave: A mmWave-based Scheme of Non-Contact and High-Definition Heart Activity Computing. *Proc. ACM Interact. Mob. Wearable Ubiquitous Technol.* 5, 3 (2021), 135:1–135:26.
- [66] Jingjing Xu, Xu Sun, Zhiyuan Zhang, Guangxiang Zhao, and Junyang Lin. 2019. Understanding and Improving Layer Normalization. In *NeurIPS*. 4383–4393.
- [67] Kaiqiang Xu, Xinchen Wan, Hao Wang, Zhenghang Ren, Xudong Liao, Decang Sun, Chaoliang Zeng, and Kai Chen. 2021. TACC: A Full-stack Cloud Computing Infrastructure for Machine Learning Tasks. *arXiv preprint arXiv:2110.01556* (2021). <https://doi.org/10.48550/ARXIV.2110.01556>
- [68] Yuzhe Yang, Kaiwen Zha, Ying-Cong Chen, Hao Wang, and Dina Katabi. 2021. Delving into Deep Imbalanced Regression. In *ICML (Proceedings of Machine Learning Research, Vol. 139)*. PMLR, 11842–11851.
- [69] Hongyi Zhang, Moustapha Cissé, Yann N. Dauphin, and David Lopez-Paz. 2018. mixup: Beyond Empirical Risk Minimization. In *ICLR (Poster)*. OpenReview.net.
- [70] Linjun Zhang, Zhun Deng, Kenji Kawaguchi, Amirata Ghorbani, and James Zou. 2021. How Does Mixup Help With Robustness and Generalization?. In *ICLR*.
- [71] Shujie Zhang, Tianyue Zheng, Zhe Chen, and Jun Luo. 2022. Can we obtain fine-grained heartbeat waveform via contact-free rf-sensing?. In *IEEE INFOCOM 2022-IEEE Conference on computer communications*. IEEE, 1759–1768.
- [72] Langcheng Zhao, Rui Lyu, Qi Lin, Anfu Zhou, Huanhuan Zhang, Huadong Ma, Jingjia Wang, Chunli Shao, and Yida Tang. 2024. mmArrhythmia: Contactless Arrhythmia Detection via mmWave Sensing. *Proc. ACM Interact. Mob. Wearable Ubiquitous Technol.* 8, 1 (2024), 30:1–30:25.
- [73] Tianyue Zheng, Zhe Chen, Shujie Zhang, Chao Cai, and Jun Luo. 2021. MoRe-Fi: Motion-robust and Fine-grained Respiration Monitoring via Deep-Learning UWB Radar. In *Sensys*. ACM, 111–124.